

# The influence of ionized gas kinematics on H<sub>II</sub> galaxies

## The cases of Tol 1004-296 and Tol 0957-278

Henri Plana,<sup>1\*</sup> Vitor G. Alves,<sup>1</sup> Maiara S. Carvalho<sup>2</sup>

<sup>1</sup>Laboratório de Astrofísica Teórica e Observacional - Departamento de Ciências Exatas - Universidade Estadual de Santa Cruz, 45662-900 Ilhéus-BA, Brazil

<sup>2</sup>Instituto de Astronomia, Geofísica e Ciências Atmosféricas Cidade Universitária, Rua do Matão, 1226 - São Paulo-SP, Brazil

Accepted XXX. Received YYY; in original form ZZZ

### ABSTRACT

Blue Compact Galaxies (BCGs), also known as H<sub>II</sub> galaxies, are dwarf, star-forming objects with relatively simple dynamics, which allows for the investigation of star formation mechanisms in a cleaner manner compared to late-type objects. In this study, we have examined various characteristics of the interstellar medium, in connection with the kinematics and dynamics of ionized gas, in Tol 1004-296 and Tol 0957-278. These two objects were observed using the SOAR Integral Field Spectrometer (SIFS) attached to the Southern Observatory for Astrophysical Research (SOAR). Both galaxies were observed with two gratings: one with medium resolution for monochromatic and abundance maps, and another with high resolution for kinematics and profile analysis. Additionally, we conducted an analysis on the velocity and velocity dispersion maps using intensity-velocity dispersion ( $I - \sigma$ ) and velocity-velocity dispersion ( $V_r - \sigma$ ) diagrams. Neither object exhibits a rotation pattern, and only Tol 1004-296 shows a velocity gradient between the two principal knots. However, the study reveals the significant role played by velocity dispersion in the star formation process. Specifically, we identified a relationship between monochromatic intensity, metallicity, and velocity dispersion, where high emission corresponds to low metallicity and low velocity dispersion. Tol 1004-296, in particular, exhibits a distinctive linear high velocity dispersion pattern between the two main knots, suggesting that both star formation sites are pushing the gas in opposite directions.

**Key words:** galaxies: kinematics and dynamics - galaxies: abundances - galaxies: dwarf - galaxies: starburst - galaxies: ISM - galaxies: individual (Tol 1004-296, Tol 0957-278)

### 1 INTRODUCTION

The concept of nuclear activity and starburst galaxies, characterized by their blue color, has been known since pioneering work by Haro et al. (1956), Ambartsumian et al. (1968), Zwicky (1964), Zwicky (1966), and Markarian et al. (1967). These objects collectively represent a diverse array of galaxies, each with unique physical and morphological characteristics. However, soon after these initial studies, a classification scheme began to emerge in the literature. Criteria such as luminosity and morphological properties were utilized to classify the galaxies observed in the aforementioned surveys. The term "Blue Compact Galaxies" (BCG), as defined by Zwicky & Zwicky (1971), refers to objects (or parts of objects) with surface brightness brighter than 20 mag arcsec<sup>-2</sup> in both blue and red plates. Thuan & Martin (1981) later referred to these objects as Blue Compact Dwarfs (BCDs), defining them as having an absolute blue magnitude fainter than  $M_B = -18.15$  mag, a diameter less than 1 kpc, and exhibiting strong emission lines superimposed on a blue continuum. Furthermore, the spectra of these objects can also serve as selection criteria. Sargent et al. (1970) published findings on "isolated extragalactic H<sub>II</sub> regions" with spectra resembling H<sub>II</sub> regions, characterized by prominent strong emission lines above a weak stellar continuum, and

morphologies consistent with BCDs. Terlevich & Melnick (1981) further investigated extragalactic H<sub>II</sub> regions, examining their chemical composition, luminosity, and velocity dispersion.

The entities now termed H<sub>II</sub> galaxies began to be studied more systematically in the 1990s. Terlevich et al. (1991) and Salzer et al. (1989a,b) presented imaging and spectrophotometric catalogs of these galaxies. The morphology of H<sub>II</sub> galaxies is diverse; while many exhibit an irregular shape, some display spiral arms and multiple bright knots indicative of intense star formation sites (Telles & Terlevich 1997a; Méndez & Esteban et al. 2000; Lagos et al. 2011).

In addition to their low luminosity ( $M_B > -18$  mag) and compactness (diameter < 1 kpc), H<sub>II</sub> galaxies also demonstrate low metallicity (between 1/50 and 1/3 of solar metallicity) (Thuan 1985).

Initially, due to their low metallicity and high EW(H $\alpha$ ), BCDs were believed to be young galaxies in the process of forming their first generation of stars. However, this hypothesis was swiftly challenged. Broadband optical and near-infrared imaging and photometry revealed the presence of an underlying older stellar population, suggesting that the intense star-forming episodes (starbursts) were merely phases followed by more prolonged and quiescent periods (Thuan 1983; Telles & Terlevich 1995; Papaderos et al. 1996a,b; Telles & Terlevich 1997a; Cairós et al. 2003; Muñoz-Mateos et al. 2009). Westera et al. (2004) and Cuisinier et al. (2006) further in-

\* E-mail: plana@uesc.br

investigated these distinct stellar populations: young, intermediate, and old.

Even though it is becoming clear that BCDs or HII galaxies are not early galaxies forming their first stars, they still offer certain advantages that make them the best objects for studying Star Formation (SF) mechanisms (Cairós et al. 2015). Their relatively simple dynamics, without spiral arms resulting from density waves and absence of disk instabilities, allows for the investigation of SF mechanisms in a cleaner manner compared to late-type objects (Hunter & Elmegreen 2004). The shallow potential well also facilitates feedback processes (MacLow & Ferrara 1999). High spatial resolution (approximately 2 – 12 pc) hydrodynamical simulations indicate that starbursts result from gas fragmentation into massive and dense clouds rather than large-scale inflows of gas (Perret et al. 2014), although this remains a topic of ongoing debate. Often referred to as "local Building Blocks," BCGs offer our best chance to understand the properties of high-redshift galaxies (Kunth et al. 2000), and they serve as ideal laboratories for studying star formation processes in massive clusters ( $> 10^4 M_{\odot}$ ) (Greis et al. 2016; Brennan et al. 2017).

The emergence of Integral Field Units (IFUs) in the 2000s has allowed for the mapping of electronic density, reddening, metallicity, ionization mechanisms, and gas kinematics of these objects. Depending on the instrument used, a trade-off between field of view and spatial sampling must be made. Over the last 15 years, several studies have been conducted using IFUs. Among them, García-Lorenzo et al. (2008), Lagos et al. (2009), Bordalo et al. (2009), Castillo-Morales et al. (2011), Cairós et al. (2015), Cairós et al. (2017a), Cairós et al. (2017b), Carvalho & Plana (2018), Cairós et al. (2020), Egorov et al. (2021) and Cairós et al. (2022) have investigated more than 15 objects using IFU instruments in various ways. The most recent studies have focused on peculiar objects such as Mrk 900, Haro 14, and DDO 53.

These studies reveal some common characteristics. Most of these galaxies are unrelaxed objects, displaying irregular morphologies with clumpy SF sites and filamentary features of the ionized gas. Nearly all objects exhibit strong differences between the gas and stellar distributions. Several galaxies contain Wolf-Rayet (WR) stars (Conti & Morris 1990). The ionization mechanisms predominantly stem from photoionization, although some objects (less than 50%) also show shock contributions in the outer regions. Extinction maps exhibit inhomogeneity. In some cases, the velocity field displays a rotation pattern (or at least a coherent velocity gradient), and the velocity dispersion maps are also inhomogeneous. Some studies of individual objects reveal two stellar populations as mentioned earlier: a very young 5.5–6.5 Myr stellar population in the SF sites and a Gyr-old population in an extended Low Surface Brightness (LSB) part of the galaxy.

The formation of BCD galaxies remains a subject of debate, with one scenario proposing interaction/fusion between low-mass, gas-rich galaxies. Chhatkuli et al. (2023) studied a sample of BCDs and found traces of dwarf-dwarf mergers. Particularly, they demonstrated the presence of a young stellar population (a few 10 Myrs old) as a result of the merger. A detailed study of a specific object, VCC 848, utilizing N-body/hydrodynamical simulations, H $\alpha$ , and Herschel PACS observations, revealed that this object is the outcome of a merger between a gas-dominated progenitor and a gas-bearing star-dominated galaxy (Zhang et al. 2020).

In this paper, we investigate two HII galaxies, Tol 1004-294 and Tol 0958-278, using the SIFS-IFU at the SOAR Telescope. We present a more detailed gas kinematics analysis of these objects to shed new light on the star formation mechanisms.

The paper is organized as follows: Section 2 presents the data, a

description of the objects, and details of the data reduction. Section 3 describes the different results obtained. Finally, Section 4 concludes the article.

## 2 THE DATA

We are presenting here two galaxies, Tol 1004-296 and Tol 0957-278 (also known as NGC 3125 and Tol 002). They are catalogued as Blue Compact Dwarf objects (Gil de Paz et al. 2005), also commonly called HII galaxies (Terlevich et al. 1991). These objects have been chosen following the criteria: (1) Presence of strong emission lines with a flux limit of  $5.0 \times 10^{-15} \text{ erg s}^{-1} \text{ cm}^{-2}$  (for [NII]6584Å) in order to have an SNR no lower than 3; (2) Low redshift in order to keep good spatial sampling; (3) Large enough in order to have the maximum number of pixels for the diagnostic diagrams (but not too large in order to be observed with a reasonable number of IFU fields); (4) Integrated velocity dispersion larger than  $30 \text{ km s}^{-1}$  (Bordalo & Telles 2011).

Both galaxies are characterised by a strong gas concentration and a high star formation rate, with a spectrum dominated by intense emission lines superimposed on a weak stellar continuum (Terlevich et al. 1991).

### 2.1 Tol 1004-296

The dwarf galaxy Tol 1004-296, also known as NGC 3125, ESO 435-G 041, ESO 100419-2941.5, AM 1004-294, MCG 05-24-022, is classified as a BCG with a magnitude of  $M_V = -17.7$  (Bergvall & Olofsson 1986) and a low metallicity of  $12 + \text{Log}(\text{O}/\text{H}) = 8.34$  (Vacca & Conti 1992). It is located at a distance of 11.99 Mpc<sup>1</sup>. Smith et al. (1976) described it as an object with super condensations showing emission lines and a diffuse stellar continuum, from an objective prism survey (Smith 1975). Spectroscopic survey by Penston et al. (1977) confirmed these objective prism data, exhibiting HeII $\lambda$ 4686 emission line in one of the condensation. Reif et al. (1982) has detected H $\alpha$  content and Paturel et al. (2003) converted it to mass according to Pustilnik & Martin (2007), giving an  $M_{HI} = 3.19 \times 10^8 M_{\odot}$ . Kunth et al. (1985) report the presence of Wolf Rayet (WR) stars in the object. Dust content and mass have been estimated to  $4.4 \times 10^5 M_{\odot}$  by Engelbracht et al. (2008), using *Spitzer Observatory*, also giving a dust temperature of  $53.7 \pm 0.3 \text{ K}$ .

Tol 1004-296 has been observed in the R, B and H $\alpha$  bands on several occasions. Kunth et al. (1988), Papaderos et al. (2002), Gil de Paz et al. (2003, 2005) present studies of this object based on images in these three bands. Kunth et al. (1988) B image mentioned four intense star formation regions. Gil de Paz et al. (2003) shows both the broad and narrow bands images of the object. It is notable that the extension of the H $\alpha$  emission goes beyond  $40''$ . We can also see that this extension, at lower limits, appears as filaments. A  $20'' \times 20''$  zoomed field of view is also presented in Gil de Paz et al. (2003) H $\alpha$  images (slightly different compared to the observed field with SIFS - see below).

The spectrum shown by Terlevich et al. (1991) is dominated by intense emission lines of hydrogen (H $\alpha$  and H $\beta$ ) and forbidden oxygen lines such as [OIII] $\lambda$ 5007 and [OIII] $\lambda$ 4959. Kehrig et al. (2004) also give the fluxes of the main emission lines from the high efficient spectrograph *FEROS* using one fibre.

<sup>1</sup> Local Group distance from Nasa Extragalactic Database

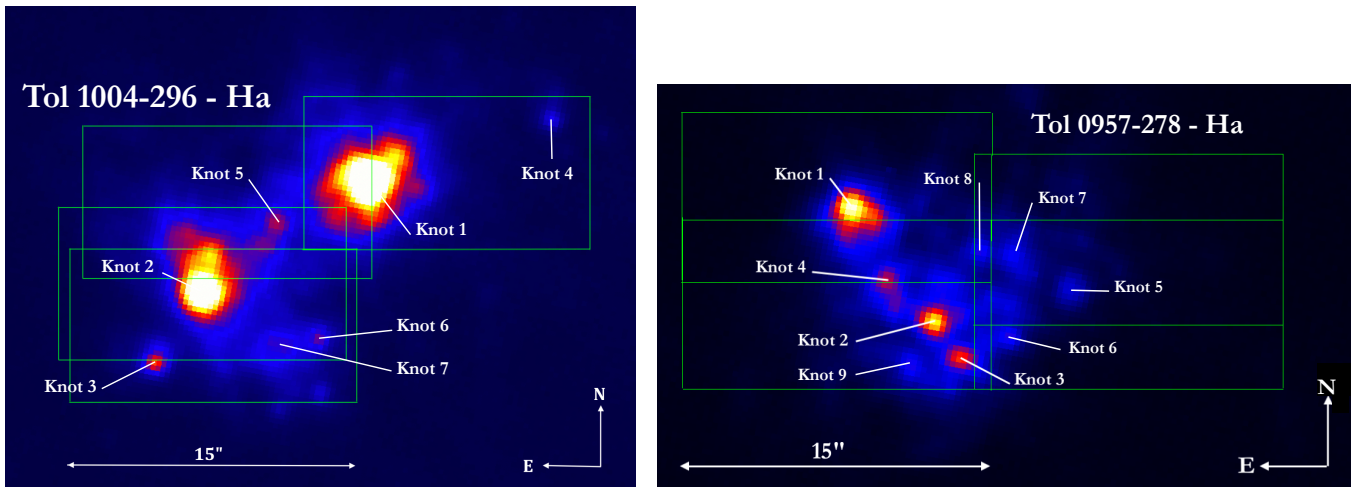


**Figure 1.**  $H\alpha$  images of Tol 1004-296 and Tol 0957-278 from the Irénée du Pont telescope at LCO Observatory.

Lagos et al. (2007) published an  $H\beta$  emission map and equivalent width (EW) image showing  $EW(H\beta)$  above  $90\text{\AA}$ . Three intense emission sites are also visible in these maps.

In Schwartz et al. (2006), low-amplitude outflows were shown through spectroscopy conducted with the HST in the two main star-forming regions of the object.

Observations in the near-infrared, using the ESO-VLT SINFONI (Eisenhauer et al. 2003), made it possible to obtain images of the continuum emission in the K-band, where a series of faint compact sources are detected near the bright central region (Vanzi et al. 2011). The SINFONI field was  $8' \times 8'$  with a resolution of  $0.250 \times 0.125$  arcsec/pixel. Vanzi et al. (2011) focused specifically on node 1 in the nomenclature of Lagos et al. (2007) and A in the nomenclature of Vacca & Conti (1992) and Stevens et al. (2002).

The galaxy is also composed of starburst regions, as well as being populated by massive star clusters that span a range of ages. Additionally, Vanzi et al. (2011) found that in several areas there is thermal bremsstrahlung emission and molecular hydrogen clouds separate from the  $HII$  regions. These regions of molecular hydrogen are mainly excited in a fluorescent manner, extending beyond the giant  $HII$  regions and outlining the shape of the molecular cloud involved in star formation Vanzi et al. (2011).

Another component of this galaxy is the presence of peaks of  $[\text{FeII}]$  emission located outside the  $HII$  regions, indicating the presence of supernovae that may have triggered starburst episodes. Vanzi et al. (2011) suggests that these episodes occurred in a chain, with the older one triggering the most recent one. This hypothesis was also raised by Cresci et al. (2010).

Both Cresci et al. (2010) and Vanzi et al. (2011) show regions where starburst episodes are occurring. However, Vanzi et al. (2011) found that the massive starburst episodes occurred in three separate episodes, resulting in the distinct intense emission sources.

The massive starburst episodes populate the galaxy with hot and young stars. However, this doesn't imply the presence of older stars in the galaxy: one characteristic of  $HII$  galaxies is the spatial dominance of young stars, making it challenging to detect older stellar populations (Westera et al. 2004).

Tol 1004-296 exhibits the strongest known emission in  $[\text{HeII}]\lambda 1640$  of stellar origin, providing important information about the most massive stars in the galaxy. In Chanda et al. (2004), a study of the massive stellar content (Wolf-Rayet stars and O stars) in Tol 1004-296 was conducted, revealing a significant predominance of

WN late-type Wolf-Rayet stars. Westera et al. (2004) and Cuisinier et al. (2006) have estimated characteristics of young, intermediate, and old stellar populations. The ratio between young + intermediate to old stellar population mass is 1:100 and the age is between 10 to 20 Myrs. And the young stellar mass to the total stellar mass ratio is 0.008. The young population age is between 1 to 2 Myrs and the old population to the total stellar mass ratio is 0.99.

## 2.2 Tol 0957-278

The galaxy Tol 0957-278, also known as Tol 02, ESO 435-IG 020, AM 0957-275, PGC 028863, was initially observed by Smith et al. (1976) and classified as a medium-strong emission line emitter. Kunth et al. (1985); Schaerer et al. (1999); Méndez & Esteban et al. (2000) also report the presence of Wolf-Rayet (WR) stars, similar to Tol 1004-296. Broadband CCD imaging from Kunth et al. (1988) and Doublier et al. (1999) confirms the clumpy shape of the object. Campbell et al. (1988)'s modeling confirms a low metallicity of  $12 + \log(O/H) = 8.1$ , consistent with what has been reported in more recent studies (Vacca & Conti 1992; Masegosa et al. 1994; Buckalew et al. 2005; Engelbracht et al. 2008).

Terlevich et al. (1991) and Masegosa et al. (1994) published emission line fluxes and ion abundances for different samples of  $HII$  galaxies, including both objects in our study. A more recent study by Kehrig et al. (2004) also provides emission line fluxes, which we used for the selection of our two targets.

Tol 0957-278 is neighbor to several other  $HII$  galaxies as mentioned by Telles & Terlevich (1995) and seems to form a pair system with ESO 435-G 016. Sung et al. (2002) saw this pair as an interacting system. Kim et al. (2017) studied the  $H I$  content of this system, estimating Tol 0957-278's extended  $H I$  gas mass to be  $1.11 \times 10^8 M_{\odot}$ . They also concluded that the system has been tidally disturbed, and the interaction is responsible for the recent star formation activities.

Tol 0957-278 has a distance of  $9.93 \text{ Mpc}^2$  and an angular extension of  $\approx 60'' \times 40''$  (Torres-Campos et al. 2017). It is also classified as a BCD galaxy due to its low B-band magnitude  $M_B = -16.26 \text{ mag}$  (Kunth et al. 1988; Doublier et al. 1999; Gil de Paz et al. 2003). Gil de Paz et al. (2003) observed it in the  $H\alpha$  band, and, similar to the

<sup>2</sup> Local Group distance from NASA Extragalactic Database

**Table 1.** Journal of Observations

Object	Right Ascension	Declination	Systemic Velocity <sup>1</sup> (km s <sup>-1</sup> )
Tol1004-296	10:06:33.30	-29:56:05.00	1113
Tol0957-278	09:59:21.50	-28:07:58.76	971
Run	Grating	Observed Fields	Exposure Time per field
January - March 2022	R700M	4	2 × 20min
February 2023	M1500M3	4	2 × 15min

<sup>1</sup> Heliocentric Velocity from NED.

previous object, Tol 0957-278 shows extended H $\alpha$  emission (25'') with a filamentary aspect on the outskirts.

Lagos et al. (2007) also published H $\beta$  emission and equivalent width (EW) images showing EW(H $\beta$ ) above 150Å. Four intense emission sites are also visible in these maps.

An underlying older stellar population mixed with a much younger stellar population has been known for quite some time, but it is still difficult to separate (Westera et al. 2004). In their study, Westera et al. (2004) and Cuisinier et al. (2006) found the following characteristics of this older population. The mass ratio between the young + intermediate population/old population is 1 to 100, the mass ratio between the young population and the total stellar mass is between 0.0081 and 0.0161. Finally, they estimated that the ratio between the old population and the total stellar mass is 0.96. The age of the young population is between 1 and 2 Myrs, and the age of the intermediate population is between 50 and 200 Myrs.

Torres-Campos et al. (2017) conducted a photometric study of the object in optical, NIR broadband filters, and narrow H $\alpha$ , [OIII] $\lambda$ 5007 filters. They identified eight star cluster complexes (SCCs). These SCCs are delineated by the H $\alpha$  emission, which is located in the central zone of the galaxy and extends towards the north and south regions. They have focused on decomposing the galaxy into a disk - or host galaxy formed by old stellar populations - and the Star Formation region (Low Surface Brightness Component - LSBC and Star Formation Component). They also estimated the ages and masses of these components. The age and masses of the LSBCs span between 3.7 Myrs to 2.5 Gyrs and  $2.4 \times 10^6 M_{\odot}$  to  $93.3 \times 10^6 M_{\odot}$ . The age and masses of the SCCs span between 3.1 Myrs to 11 Myrs and  $35.5 \times 10^3 M_{\odot}$  to  $269.1 \times 10^3 M_{\odot}$ .

### 2.3 Observations

These two objects were observed at the SOAR Observatory<sup>3</sup> using the SIFS (Lepine et al. 2003; Fraga 2018) instrument<sup>4</sup>. SIFS is an Integral Field Unit (IFU) spectrograph. The instrument has a spatial scale of 0.3'' per fiber, and the field of view is 15'' × 7.8''. The fibers feed a pseudo slit to a bench spectrograph. The detector is a 4096 × 4112 pixel CCD231-84 from E2V with a pixel physical size of 15  $\mu\text{m}^2$ . The Read-Out Noise (RON) of the detector is 2.0 e-/ADU.

Several observations were necessary to cover the targets. We used four different fields for each target resulting to a final field of view of 30'' × 15''. Each target was observed with two different gratings: the 700R (with a resolution of 4200@5500) was used for obtaining monochromatic maps for different emission lines, and the 1500M3

(with a resolution of 9500@5500) for the velocity and velocity dispersion maps. Table 1 shows the observation log. Figure 1 illustrates the different fields using an H $\alpha$  image from the Irénée du Pont telescope at La Campanas Observatory<sup>5</sup> for both galaxies. We also show the main emission knots.

We estimated a precision equivalent to a spaxel (0.3'') in the reconstruction of the mosaics. Observations couldn't be completed in a single semester and had to be spread out over two semesters, a year apart.

During the night, two spectrophotometric standard stars were also observed: LTT 3218 and EG 274 (Hamuy et al. 1993), for flux calibration purposes.

We are also presenting data from the MUSE (Bacon et al. 2010) instrument attached to the ESO-VLT for Tol 1004-296. The observation was part of proposal ID 094.B-0745 (PI - Garcia-Benito, R.). The MUSE instrument has the great advantage of having a large Field of View (FoV) equal to  $\approx 1.0' \times 1.0'$ , allowing the observation of the entire object in a single 2880s observation. The spatial sampling is 0.2'' per pixel. On the other hand, the available grating only provides a spectral resolving power of 1770@4800Å.

### 2.4 Data reduction

#### 2.4.1 Preliminary Reduction

The initial stage of data reduction, comprising bias correction, flat field correction, identification of lenses, and cube building, was conducted at the Laboratório Nacional de Astrofísica - LNA office. Wavelength calibration was also performed at LNA. The office sent us individual data cubes wavelength calibrated for each field for the two galaxies.

The first step was to construct a mosaic consisting of the four observed fields for each object.

Flux calibration was performed using the two spectrophotometric stars, LTT 3218 and EG 274, and the *standard, sensfunc, calibrate* tasks from IRAF<sup>6</sup>.

### 2.5 Moment Maps

The subsequent step involved extracting sub-cubes for each of the targeted emission lines. Depending on the lines, the data cube depth had between 30 or 40 spectral pixels, sufficient to determine the continuum level. To account for seeing effects, we applied a light spatial Gaussian smoothing of 3 spaxels (equivalent to 0.9'') Full Width at Half Maximum (FWHM).

Next, we generated various moment maps using two different techniques: an in-house macro and a Gaussian profile fitting technique.

- **Monochromatic and Continuum Maps:** For each sub-cube, we identified the peak emission and isolated the profile. Then, we performed a linear fit of the remaining continuum and removed it from the sub-cube. Subsequently, we collapsed it to obtain monochromatic maps in different emission lines. We also generated continuum maps by removing the prominent emission lines and collapsing the cube, particularly for the MUSE data where the quality was better.

- **Radial Velocity Maps:** To produce the velocity map, we isolated

<sup>3</sup> Southern Observatory for Astrophysical Research

<sup>4</sup> SOAR Integral Field Spectrometer

<sup>5</sup> These images were downloaded from the NED website

<sup>6</sup> IRAF - Image Reduction and Analysis Facility - Tody (1986)

the profile as described before and estimated the barycenter<sup>7</sup> of the profile to account for possible asymmetries.

- **Velocity Dispersion Maps:** The velocity dispersion map was derived from the FWHM of the isolated profile. The FWHM was then transformed into dispersion using the formula  $\sigma = \frac{FWHM}{2\sqrt{2\ln 2}}$ .

The velocity dispersion was corrected for thermal<sup>8</sup> and instrumental broadening following the formula.

$$\sigma = \sqrt{\sigma_{obs}^2 - \sigma_{th}^2 - \sigma_{inst}^2}$$

The thermal dispersion,  $\sigma_{th}$ , was estimated to be  $9.32 \text{ km s}^{-1}$  for hydrogen at a temperature of  $10^4 \text{ K}$ . We estimated the instrumental broadening using the calibration lamp observation, giving  $\sigma_{inst} = 13.0 \pm 3 \text{ km s}^{-1}$ .

Additionally, we used a Gaussian fit macro to cross-verify our results. However, we opted to retain the technique described above for estimating the velocity maps and velocity dispersion, as it allows for the consideration of possible asymmetries in the profiles.

## 3 RESULTS

### 3.1 Emission lines maps

We were able to produce monochromatic maps of the following emission lines:  $H\beta\lambda 4861$ ,  $[OIII]\lambda\lambda 4959, 5007$ ,  $HeI\lambda 5876$ ,  $[NII]\lambda 6548$ ,  $H\alpha\lambda 6563$ ,  $[NII]\lambda 6584$ ,  $[SII]\lambda\lambda 6716, 6732$ ,  $HeI\lambda 6678$ ,  $[ArIII]\lambda 7136$ . Figure 2 to Figure 4 present these different monochromatic maps for both objects (except that for Tol 0957-278, where  $[HeI]\lambda 5876$ ,  $[NII]\lambda 6548$ ,  $[HeI]\lambda 6678$  and  $[ArIII]\lambda 7136$  lines were too weak to be extracted). Table 2 and Table 3 summarize the fluxes of the different emission lines in the different emission knots (they also include several others quantities such as diagnostic line ratios, oxygen abundances, interstellar extinction, radial velocity and velocity dispersion). These knots are symbolically shown in Figure 2 ( $H\alpha$  map) and Figure 4 ( $H\alpha$  map). We estimated these regions by limiting the extension where the SNR is above 5 in the  $H\alpha$  line. In Figure A1, we have added several histograms representing the distribution of several parameters ( $[SII]\lambda 6716/[SII]\lambda 6731$ ,  $EW(H\beta)$ ,  $E(B-V)$  and diagnostics diagrams line ratios).

In Tol 1004-296 case, we recognised the two large knots (Knot 1 and 2) separated by  $10.3''$  (661 pc), visible in Figure 1.

It is noticeable that only the two largest bright sites appear weaker in others emission wavelengths, such as  $[NII]\lambda 6584$ ,  $[SII]\lambda 6716$ ,  $[SII]\lambda 6716$ ,  $[HeI]\lambda 5876$ ,  $[NII]\lambda 6548$ ,  $[HeI]\lambda 6678$  and  $[ArIII]\lambda 7136$ . We can also notice that the Knot 7 has a more elongated shape or formed by two sub nuclei in  $[OIII]\lambda 5007$  or  $H\alpha$ .

The monochromatic maps from the MUSE data are available in Figures B1. Extension of the ionized gas is, as expected, much larger compared to our SIFS data. For the brightest emission lines ( $H\alpha$ ,  $H\beta$ ,  $[OIII]\lambda\lambda 4959, 5007$ ), the extension is  $50'' \times 50''$  (we limit the emission to a Signal to Noise Ratio (SNR) superior to 8, in order to keep the filamentary character of the emission, in the outskirts, without the sky background noise). It is more or less the same extension showed by Gil de Paz et al. (2003) with the narrow band imaging of the  $H\alpha + [NII]$  emission. The MUSE data show the following emission lines:

$H\beta\lambda 4861$ ,  $[OIII]\lambda\lambda 4959, 5007$ ,  $HeI\lambda 5876$ ,  $[OI]\lambda 6300$ ,  $[NII]\lambda 6548$ ,  $H\alpha\lambda 6563$ ,  $[NII]\lambda 6584$ ,  $[SII]\lambda\lambda 6716, 6732$ ,  $HeI\lambda 6678$ ,  $[ArIII]\lambda 7136$ . We easily recognise the different Knots we have presented previously.

Tol 0957-278 maps show a more complex morphology (Figure 4), nine emission sites can be seen on the  $[OIII]\lambda 4959$  and  $[OIII]\lambda 5007$  lines.  $H\alpha$  map in Figure 4 shows the location of emission sites in the galaxy. Four knots (1, 2, 3 and 4) are brighter than the other five knots (5, 6, 7, 8 and 9).

### 3.2 Electron density and electron temperature

#### 3.2.1 Electron density

In order to estimate the abundances, it is first necessary to estimate the electronic density and temperature. The electron density is obtained using the emission line ratio  $[SII]\lambda 6717 / [SII]\lambda 6731$  and using the task TEMDEM, based on the FIVEL program (Shaw et al. 1995), which is included in the IRAF package NEBULAR. We also used the PyNeb code Luridiana et al. (2015).  $[SII]\lambda 6717 / [SII]\lambda 6731$  maps are presented in Figure 5 for both objects. The ratio is between  $0.7 \pm 0.1$  and  $1.8 \pm 0.1$  or Tol 1004-296 (some hot pixels have a value up to 3.5) and between  $0.65 \pm 0.1$  and  $1.95 \pm 0.1$  for Tol 0957-278 (here too, some hot pixels have values up to 3.5). The center of Knots 1 and 2 of Tol 1004-296 have lower values compared to values around. In Tol 0957-278 case too, emission knots show lower ratio compared to values around. This gives an electron density  $80 \text{ cm}^{-3} < n_e < 400 \text{ cm}^{-3}$ . Following the low regime Osterbrock & Ferland (2006), we assume the electron density  $n_e = 100 \text{ cm}^{-3}$  for both galaxies (Lagos et al. 2009; García-Lorenzo et al. 2008; Cairós et al. 2020, 2022).

#### 3.2.2 Electron temperature

The electron temperature,  $T_e$  is usually estimated using the oxygen emission line, with  $[OIII]\lambda\lambda 4959, 5007 / [OIII]\lambda 4363$  ratio and one of the code mentioned above (NEBULAR or Pyneb). The  $[OIII]\lambda 4363$  is outside our spectral range. We decided to use the values of these lines available in Kehrig et al. (2004). For both galaxies, Kehrig et al. (2004) is giving three values (center, NW and SE), we then used PyNeb to estimate the electron temperature, assuming a  $n_e = 100 \text{ cm}^{-3}$ . Table 4 summarises the different values for both objects.

PyNeb (Luridiana et al. 2015) also allowed us to diagnose the electron density and temperature. With the values of the  $[OIII]\lambda\lambda 4959, 5007 / [OIII]\lambda 4363$  and  $[SII]\lambda 6717 / [SII]\lambda 6731$  ratios from Kehrig et al. (2004), it was possible to have an  $T_e$  vs  $n_e$  graph with the  $[OIII]$  lines and  $[SII]$  ratios. This graph is compatible with the use of a constant  $n_e = 100 \text{ cm}^{-3}$  and  $T_e = 10^4 \text{ K}$ .

Figure B2 shows the  $[SII]\lambda 6716/[SII]\lambda 6732$  lines ratio for Tol 1004-296 observed with MUSE. In the center, corresponding to the SIFS FoV, Knot 1 and Knot 2 show respectively  $1.25 \pm 0.07$  and  $1.29 \pm 0.04$ .

the ratio is between 1.15 and 1.4. The minimum ratio corresponds to the two principals emission knots (Knots 1 and 2).

### 3.3 Interstellar extinction

Dust extinction has to be estimated and then applied to the observed fluxes in order to have correct fluxes. Interstellar extinction in nebula is computed using the observed Balmer decrement. The intrinsic luminosity,  $L_{int}$  in a given wavelength can be written as:

<sup>7</sup> It is estimated from histogram of line width, with the weight being the area of each rectangle forming the profile. More details in Amram (1991)

<sup>8</sup> See Rybicki & Lightman (2004)

**Table 2.** Intensity ratios (corrected from extinction), normalized to  $H\beta$ , interstellar extinction, diagnostic line ratios, densities, oxygen abundances, radial velocity and velocity dispersion, for the emission knots.

Ion	Knot 1	Knot 2	Knot 3	Knot 4	Knot 5	Knot 6	Knot 7
4861 $H\beta$	1.00	1.00	1.00	1.00	1.00	1.00	1.00
4959 [OIII]	$1.70 \pm 0.01$	$1.42 \pm 0.01$	$1.51 \pm 0.04$	$1.07 \pm 0.08$	$1.30 \pm 0.02$	$1.57 \pm 0.05$	$1.11 \pm 0.02$
5007 [OIII]	$5.13 \pm 0.04$	$4.22 \pm 0.03$	$4.70 \pm 0.12$	$2.96 \pm 0.23$	$3.75 \pm 0.05$	$4.37 \pm 0.14$	$3.40 \pm 0.06$
6548 [NII]	$0.04 \pm 0.01$	$0.04 \pm 0.01$	$0.02 \pm 0.01$	$0.09 \pm 0.01$	$0.03 \pm 0.01$	$0.03 \pm 0.02$	$0.03 \pm 0.01$
6563 $H\alpha$	$2.51 \pm 0.02$	$2.51 \pm 0.02$	$2.51 \pm 0.06$	$2.51 \pm 0.16$	$2.51 \pm 0.03$	$2.51 \pm 0.07$	$2.51 \pm 0.04$
6583 [NII]	$0.13 \pm 0.01$	$0.16 \pm 0.01$	$0.12 \pm 0.01$	$0.13 \pm 0.01$	$0.13 \pm 0.01$	$0.12 \pm 0.02$	$0.21 \pm 0.02$
6713 [SII]	$0.12 \pm 0.01$	$0.17 \pm 0.01$	$0.17 \pm 0.02$	$0.24 \pm 0.02$	$0.16 \pm 0.01$	$0.10 \pm 0.01$	$0.23 \pm 0.01$
6732 [SII]	$0.10 \pm 0.01$	$0.13 \pm 0.01$	$0.12 \pm 0.02$	$0.18 \pm 0.01$	$0.13 \pm 0.02$	$0.07 \pm 0.01$	$0.17 \pm 0.02$
$F(H\beta)^1$	$99.69 \pm 0.37$	$55.71 \pm 0.18$	$3.50 \pm 0.04$	$0.87 \pm 0.03$	$2.86 \pm 0.02$	$0.87 \pm 0.01$	$1.99 \pm 0.02$
$EW(H\beta)^2$	$68.31 \pm 0.12$	$76.32 \pm 0.13$	$62.06 \pm 0.40$	$48.48 \pm 0.75$	$63.20 \pm 0.24$	$61.32 \pm 0.70$	$61.32 \pm 0.7$
$E(B-V)$	$0.34 \pm 0.03$	$0.313 \pm 0.017$	$0.304 \pm 0.037$	$0.178 \pm 0.078$	$0.270 \pm 0.030$	$0.209 \pm 0.052$	$0.333 \pm 0.044$
<b>Parameters</b>	<b>Knot 1</b>	<b>Knot 2</b>	<b>Knot 3</b>	<b>Knot 4</b>	<b>Knot 5</b>	<b>Knot 6</b>	<b>Knot 7</b>
$\log([OIII]5007/H\beta)$	$0.65 \pm 0.07$	$0.59 \pm 0.04$	$0.65 \pm 0.05$	$0.48 \pm 0.08$	$0.57 \pm 0.02$	$0.63 \pm 0.02$	$0.52 \pm 0.03$
$\log([NII]6583/H\alpha)$	$-1.16 \pm 0.07$	$-1.21 \pm 0.13$	$-1.33 \pm 0.13$	$-1.27 \pm 0.17$	$-1.23 \pm 0.07$	$-1.27 \pm 0.08$	$-1.01 \pm 0.09$
$\log([SII]6716\ 6732/H\alpha)$	$-0.93 \pm 0.17$	$-0.86 \pm 0.11$	$-0.93 \pm 0.10$	$-0.80 \pm 0.21$	$-0.90 \pm 0.05$	$-1.17 \pm 0.16$	$-0.77 \pm 0.07$
$n_e$ ( $\text{cm}^{-3}$ )	< 100	< 100	< 100	< 100	< 100	< 100	< 100
$12+\log(O/H)$ (S Calibrator) <sup>3</sup>	$8.14 \pm 0.04$	$8.14 \pm 0.02$	$8.10 \pm 0.06$	$8.14 \pm 0.23$	$8.07 \pm 0.04$	$8.12 \pm 0.09$	$8.26 \pm 0.12$
$12+\log(O/H)$ (O3N2 Calibrator) <sup>4</sup>	$8.06 \pm 0.02$	$8.12 \pm 0.02$	$8.10 \pm 0.03$	$8.15 \pm 0.04$	$8.14 \pm 0.01$	$8.12 \pm 0.02$	$8.19 \pm 0.01$
$12+\log(O/H)$ (N2 Calibrator) <sup>5</sup>	$8.08 \pm 0.03$	$8.16 \pm 0.03$	$8.16 \pm 0.03$	$8.12 \pm 0.03$	$8.16 \pm 0.02$	$8.14 \pm 0.05$	$8.26 \pm 0.03$
<b>Kinematics</b>	<b>Knot 1</b>	<b>Knot 2</b>	<b>Knot 3</b>	<b>Knot 4</b>	<b>Knot 5</b>	<b>Knot 6</b>	<b>Knot 7</b>
Radial Velocity ( $\text{km s}^{-1}$ )	$1137.0 \pm 5.0$	$1162.0 \pm 4.0$	$1175.0 \pm 5.0$	$1205.0 \pm 6.0$	$1147.0 \pm 4.0$	$1176.0 \pm 6.0$	$1185.0 \pm 7.0$
Velocity Dispersion ( $\text{km s}^{-1}$ )	$31.0 \pm 2.0$	$34.0 \pm 2.0$	$20.0 \pm 2.0$	$17.0 \pm 5.0$	$28.0 \pm 2.0$	$20.0 \pm 2.0$	$25.0 \pm 2.0$

Notes: <sup>1</sup>:  $H\beta$  fluxes in  $10^{-14}$  erg  $\text{s}^{-1}$   $\text{cm}^{-2}$ . <sup>2</sup> In  $\text{\AA}$ . <sup>3</sup> S Calibrator Oxygen abundance from Pilyugin & Grebel (2016). <sup>4</sup> O3N2 Calibrator from Marino et al. (2013). <sup>5</sup> N2 Calibrator from Marino et al. (2013).

**Table 3.** Intensity ratios (corrected from extinction), normalized to  $H\beta$ , interstellar extinction, diagnostic line ratios, densities, oxygen abundances, radial velocity and velocity dispersion, for the emission knots.

Ion	Knot 1	Knot 2	Knot 3	Knot 4	Knot 5	Knot 6	Knot 7	Knot 8	Knot 9
4861 $H\beta$	1.00	1.00	1.00	1.00	1.00	1.00	1.00	1.00	1.00
4959 [OIII]	$1.38 \pm 0.02$	$2.00 \pm 0.04$	$1.88 \pm 0.04$	$1.44 \pm 0.01$	$1.44 \pm 0.02$	$1.42 \pm 0.02$	$1.43 \pm 0.02$	$1.64 \pm 0.04$	$1.73 \pm 0.06$
5007 [OIII]	$4.31 \pm 0.05$	$6.47 \pm 0.13$	$5.73 \pm 0.13$	$4.44 \pm 0.04$	$4.28 \pm 0.07$	$4.53 \pm 0.06$	$4.48 \pm 0.05$	$4.82 \pm 0.10$	$5.21 \pm 0.19$
6563 $H\alpha$	$3.06 \pm 0.03$	$3.06 \pm 0.05$	$3.06 \pm 0.06$	$3.06 \pm 0.03$	$3.06 \pm 0.04$	$3.06 \pm 0.03$	$3.06 \pm 0.03$	$3.06 \pm 0.06$	$3.06 \pm 0.10$
6583 [NII]	$0.12 \pm 0.01$	$0.46 \pm 0.01$	$0.06 \pm 0.01$	$0.12 \pm 0.01$	$0.10 \pm 0.02$	$0.09 \pm 0.01$	$0.12 \pm 0.02$	$0.09 \pm 0.01$	$0.15 \pm 0.01$
6713 [SII]	$0.21 \pm 0.02$	$0.08 \pm 0.01$	$0.18 \pm 0.01$	$0.22 \pm 0.02$	$0.19 \pm 0.01$	$0.21 \pm 0.01$	$0.28 \pm 0.03$	$0.21 \pm 0.02$	$0.16 \pm 0.02$
6732 [SII]	$0.14 \pm 0.01$	$0.08 \pm 0.02$	$0.08 \pm 0.01$	$0.14 \pm 0.01$	$0.11 \pm 0.02$	$0.15 \pm 0.01$	$0.20 \pm 0.02$	$0.16 \pm 0.02$	$0.10 \pm 0.01$
$F(H\beta)^1$	$18.77 \pm 0.11$	$4.81 \pm 0.04$	$2.89 \pm 0.03$	$4.21 \pm 0.02$	$1.23 \pm 0.01$	$2.37 \pm 0.01$	$3.08 \pm 0.02$	$1.69 \pm 0.02$	$0.82 \pm 0.01$
$EW(H\beta)^2$	$65.16 \pm 0.06$	$67.54 \pm 0.07$	$34.96 \pm 0.13$	$39.95 \pm 0.03$	$34.11 \pm 0.04$	$34.28 \pm 0.06$	$32.28 \pm 0.06$	$32.813 \pm 0.07$	$34.19 \pm 0.07$
$E(B-V)$	$0.511 \pm 0.10$	$0.33 \pm 0.03$	$0.48 \pm 0.04$	$0.36 \pm 0.03$	$0.33 \pm 0.03$	$0.41 \pm 0.04$	$0.41 \pm 0.05$	$0.45 \pm 0.07$	$0.34 \pm 0.04$
<b>Parameters</b>	<b>Knot 1</b>	<b>Knot 2</b>	<b>Knot 3</b>	<b>Knot 4</b>	<b>Knot 5</b>	<b>Knot 6</b>	<b>Knot 7</b>	<b>Knot 8</b>	<b>Knot 9</b>
$\log([OIII]5007/H\beta)$	$0.63 \pm 0.05$	$0.78 \pm 0.07$	$0.75 \pm 0.03$	$0.64 \pm 0.04$	$0.63 \pm 0.02$	$0.75 \pm 0.03$	$0.64 \pm 0.04$	$0.68 \pm 0.03$	$0.71 \pm 0.02$
$\log([NII]6583/H\alpha)$	$-1.39 \pm 0.09$	$-1.45 \pm 0.09$	$-1.47 \pm 0.09$	$-1.39 \pm 0.07$	$-1.45 \pm 0.07$	$-1.44 \pm 0.10$	$-1.37 \pm 0.11$	$-1.41 \pm 0.08$	$-1.31 \pm 0.16$
$\log([SII]6716\ 6732/H\alpha)$	$-0.93 \pm 0.06$	$-1.22 \pm 0.13$	$-1.14 \pm 0.09$	$-0.94 \pm 0.07$	$-0.10 \pm 0.09$	$-0.92 \pm 0.07$	$-0.80 \pm 0.07$	$-0.95 \pm 0.12$	$-1.07 \pm 0.08$
$n_e$ ( $\text{cm}^{-3}$ )	< 100	< 100	< 100	< 100	< 100	< 100	< 100	< 100	< 100
$12+\log(O/H)$ (N2 Calibrator) <sup>3</sup>	$8.09 \pm 0.02$	$7.84 \pm 0.16$	$8.00 \pm 0.13$	$8.11 \pm 0.04$	$8.07 \pm 0.04$	$8.05 \pm 0.11$	$8.09 \pm 0.12$	$7.95 \pm 0.21$	$8.14 \pm 0.08$
<b>Kinematics</b>	<b>Knot 1</b>	<b>Knot 2</b>	<b>Knot 3</b>	<b>Knot 4</b>	<b>Knot 5</b>	<b>Knot 6</b>	<b>Knot 7</b>	<b>Knot 8</b>	<b>Knot 9</b>
Radial Velocity ( $\text{km s}^{-1}$ )	$1041.0 \pm 5.0$	$1016.0 \pm 4.0$	$1027.0 \pm 5.0$	$1030.4 \pm 34.0$	$1032.0 \pm 3.0$	$1029.0 \pm 5.0$	$1030.0 \pm 4.0$	$1029.0 \pm 5.0$	$1025.0 \pm 4.0$
Velocity Dispersion ( $\text{km s}^{-1}$ )	$21.0 \pm 3.0$	$20.0 \pm 3.0$	$22.0 \pm 2.0$	$27.0 \pm 3.0$	$20.0 \pm 2.0$	$23.5 \pm 3.0$	$24.0 \pm 2.0$	$26.0 \pm 3.0$	$24.0 \pm 3.0$

Notes: <sup>1</sup>:  $H\beta$  fluxes in  $10^{-14}$  erg  $\text{s}^{-1}$   $\text{cm}^{-2}$ . In  $\text{\AA}$ . <sup>3</sup> N2 Calibrator from Marino et al. (2013).

**Table 4.** Electron Temperature

Name	$[OIII]\lambda\lambda 4959, 5007 / [OIII]\lambda 4363$	$T_e$ (K)
To11004-296	180.93	10511
To11004-296(NW)	199.56	10193
To11004-296(SE)	170.36	10716
To10957-278	107.87	12580
To10957-278(NW)	140.34	11435
To10957-278(SE)	73.730	14710

$$L_{int}(\lambda) = L_{obs}(\lambda) 10^{0.4k(\lambda)E(B-V)}$$

with  $L_{obs}(\lambda)$  the observed luminosity,  $k(\lambda)$  the extinction law and  $E(B-V)$  the color excess (Calzetti et al. 1994; Domínguez et al. 2013). We used the Calzetti et al. (2000) extinction law for  $k(\lambda)$  and the color excess  $E(B-V)$  has been derived from the Balmer decrement using  $H\alpha$  and  $H\beta$  lines by:

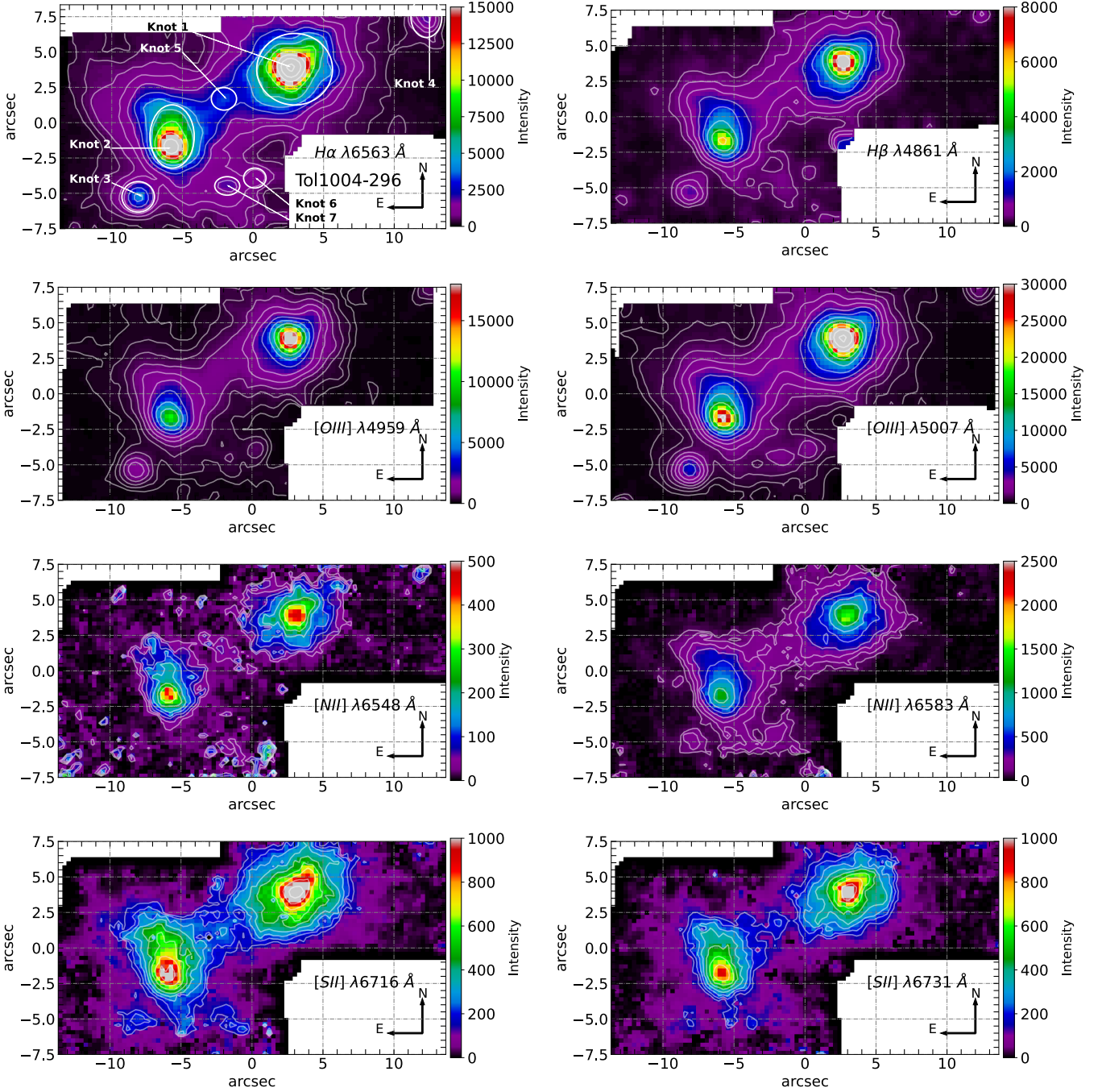


Figure 2. Monochromatic maps for Tol 1004-296.

$$\begin{aligned}
 E(B-V) &= \frac{E(H\beta - H\alpha)}{k(\lambda_{H\beta}) - k(\lambda_{H\alpha})} \\
 &= \frac{2.5}{k(\lambda_{H\beta}) - k(\lambda_{H\alpha})} \log_{10} \left[ \frac{(H\alpha/H\beta)_{obs}}{(H\alpha/H\beta)_{int}} \right]
 \end{aligned}$$

with  $k(\lambda_{H\beta})$  and  $k(\lambda_{H\alpha})$  the extinction coefficients for  $H\beta$  and  $H\alpha$ .

Adopting the theoretical ratio of 2.86 (case B recombination at a

temperature of  $10^4$  K; see Osterbrock & Ferland (2006)), the color excess is:

$$E(B-V) = 1.97 \log_{10} \left[ \left( \frac{H\alpha}{H\beta} \right)_{obs} \cdot \frac{1}{2.86} \right]$$

Figure 6 shows  $H\alpha/H\beta$  ratio maps for both objects. For Tol 1004-296, the ratio is more or less uniform around  $3.8 \pm 0.4$  with some fluctuation. Some hot spots are visible where the emission is higher (where the strong emission sites are), as for the Knot 1 (where the

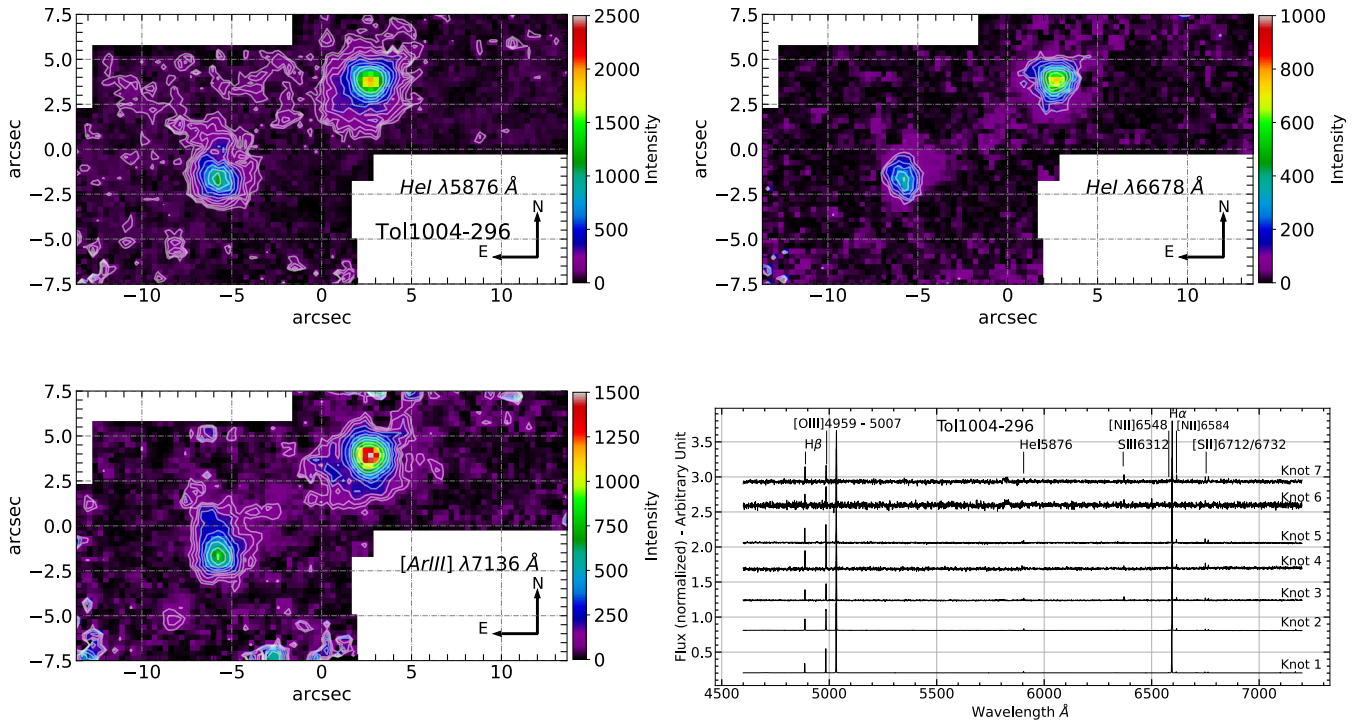


**Figure 3.** Monochromatic maps for Tol 1004-296 and integrated spectra of the seven emission knots. Each spectrum represent a  $3 \times 3$  integrated spaxels.

ratio is  $4.3 \pm 0.2$ ), the Knot 2 (where the ratio is  $4.2 \pm 0.1$ ) and the Knot 3 (where the ratio is  $4.0 \pm 0.3$ ).

For Tol 0957-278, the average ratio is around  $4.3 \pm 0.9$ . It is notable that the Knot 1 shows a value of  $5.7 \pm 0.5$  and  $3.4''$  East, the ratio goes down to  $2 \pm 0.4$ . It is possible that this difference is coming from a dust lane, present in this area.

Figure B2 shows the  $H\alpha/H\beta$  line ratio for Tol 1004-296 observed with MUSE. The line ratio inside the SIFS FoV is consistent with the map from the SIFS data.

### 3.4 Chemical abundances

It wasn't possible to use the direct  $T_e$  method (e.g. [Dinerstein et al. 1990](#); [McCall et al. 1985](#)), to determine the oxygen abundance because 1) the auroral lines such as  $[\text{O III}]\lambda 4363$  and  $[\text{N II}]\lambda 5755$  were too weak to be detected and 2) the  $[\text{O II}]\lambda\lambda 3727, 3729$  doublet and  $[\text{O II}]\lambda\lambda 7320, 7331$  lines are outside of the SIFS spectral range. However, several studies (e.g. [Pilyugin et al. 2012](#); [Pilyugin & Grebel 2016](#); [Marino et al. 2013](#); [Denicoló et al. 2002](#)) offer a series of calibrators in order to estimate the oxygen abundance using a variety of available emission lines and based on statistical studies.

[Denicoló et al. \(2002\)](#) and [Marino et al. \(2013\)](#) give the so-called  $N2$  calibrator based on the  $[\text{N II}]\lambda 6584 / H\alpha$  line ratio, with slightly different regression coefficients. First introduced by [Alloin et al. \(1979\)](#), [Marino et al. \(2013\)](#) detailed the so-called  $O3N2$  calibrator based on the  $[\text{O III}]\lambda 5007 / H\beta \times H\alpha / [\text{N II}]\lambda 6584$  using the CALIFA survey. Introduced by [Pilyugin & Grebel \(2016\)](#), the so-called  $S$  calibrator used the ratios  $([\text{N II}]\lambda 6548 + 6583) / H\beta$ ,  $([\text{S II}]\lambda 6717 + 6732) / H\beta$  and  $([\text{O III}]\lambda 4959 + 5007) / H\beta$  to derive the oxygen abundance. It's important to note from its definition that the  $S$  calibrator depends on the reddening correction.

For Tol 1004-296, we were able to implement the three methods.

Figures 7a, b, and c are respectively using the  $S$  calibrator, the  $O3N2$  calibrator, and  $N2$  calibrator. Even if the overall aspect of the maps are similar, showing gradient between the different knots, we can notice some differences between the different methods. The  $S$  calibrator (Fig. 7a) shows the greater contrast in the map between different parts of the galaxy. Even if it's not the minimum of metallicity, the Knots 1, 2, and 3 show respectively a metallicity of  $8.14 \pm 0.04$  dex,  $8.14 \pm 0.02$  dex, and  $8.10 \pm 0.06$  dex. On the outskirts (at  $2.8''$  from the Knots centers) the metallicity is higher, from  $8.20 \pm 0.05$  dex, to  $8.55 \pm 0.05$  dex. On the other hand, the  $O3N2$  calibrator (Fig. 7b) gives a lower amplitude between the metallicity in the emission knots and around them (the highest metallicity values do not exceed  $8.22 \pm 0.04$  dex.). Finally, the  $N2$  calibrator shows, in a clearer way, that higher metallicity is surrounding the emission knots.

We can notice that the metallicity of the different emission knots is between  $8.06 \pm 0.03$  dex, and  $8.16 \pm 0.04$  dex, except in Knot 7 (where it is  $8.26 \pm 0.3$  dex). It is worth notice that a lower metallicity seems to be present where the emission is higher. This is more noticeable for the Knot 1 and 2 and when looking at the calibrators  $O3N2$  and  $N2$ .

Figure B2 shows the metallicity map (using the  $S$  calibrator) for the MUSE data of Tol 1004-296. It can be noticed that the metallicity is slightly higher on the outskirts of the galaxy. In the center of the galaxy (essentially the field of view of the SIFS data), the metallicity ranges between  $8.07 \pm 0.04$  dex and  $8.30 \pm 0.04$  dex. As mentioned before, we also observed that lower metallicity corresponds to high emission knots. All seven emission knots (see Fig. 2) correspond to a minimum metallicity value.

In Tol 0957-278 case, we have implemented the  $N2$  and  $O3N2$  calibrators from [Marino et al. \(2013\)](#) (because the  $[\text{N II}]\lambda 6548$  line was too weak to be detected). Figure 7d shows the metallicity deduced from the  $N2$  calibrator. It is clear here that the metallicity is lower

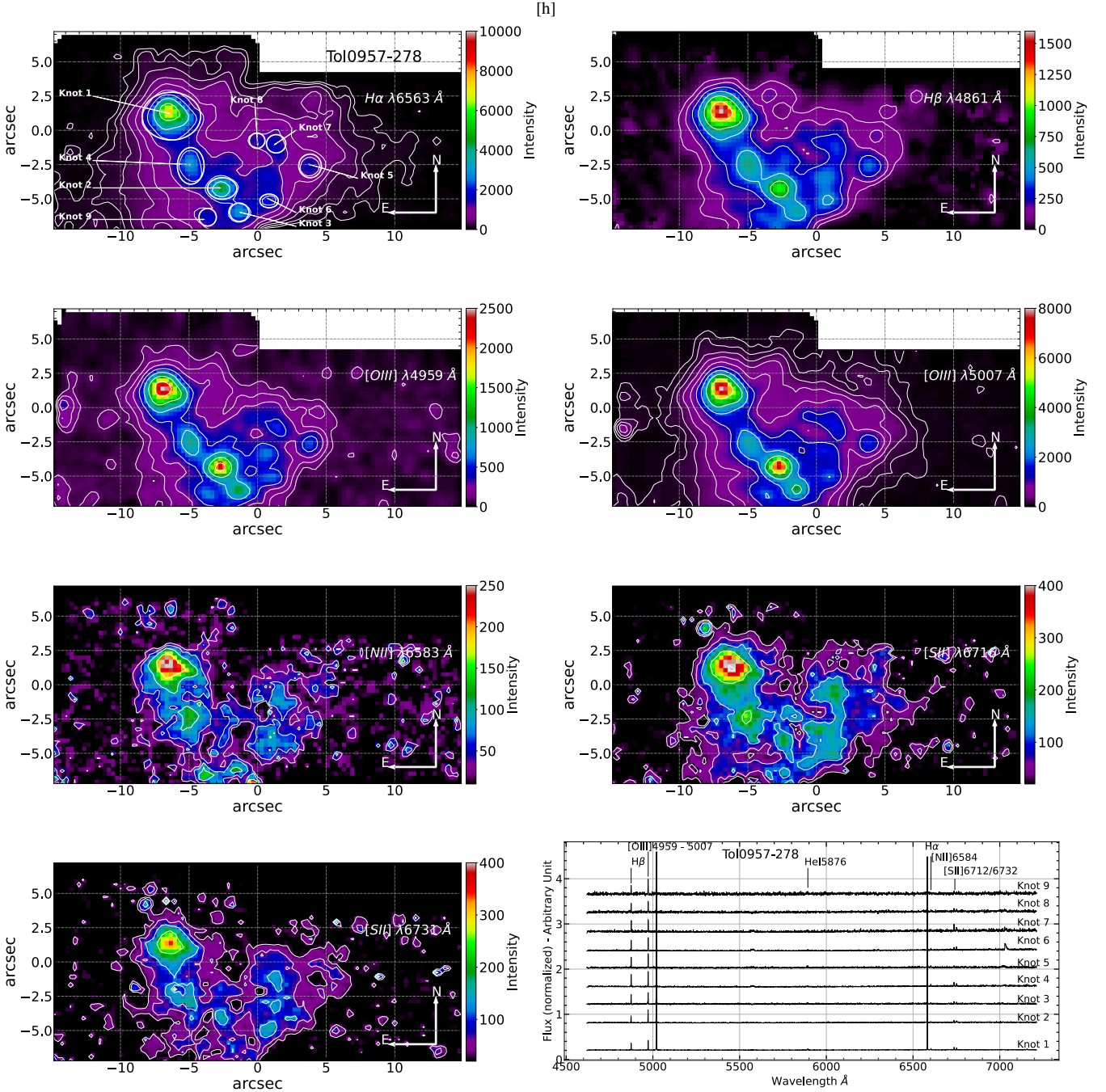


**Figure 4.** Monochromatic maps for Tol 0957-278 and integrated spectra of the nine emission knots. Each spectrum represent a 3×3 integrated spaxels.

where the emission is higher. The lowest metallicity is  $7.84 \pm 0.16$  dex in Knot 2. The brightest site (Knot 1) has a metallicity of  $8.09 \pm 0.02$  dex. Around Knot 1 (at a radius of  $1.8''$  from the brightest spot), the metallicity ranges between  $8.18 \pm 0.02$  dex and  $8.25 \pm 0.03$  dex.

### 3.5 Ionization mechanism

Photoionization from UV photons coming from hot stars, photoionization from an AGN source, or shocks from collisions (from stellar winds and supernovae (Dopita et al. 2003)), are the three ionization mechanisms could be present in an emission-line system. Baldwin et

al. (1981) and Veilleux & Osterbrock (1987) came up with a series of excitation-dependent line ratios, the so-called ionization diagnostic diagrams. The three diagnostic plots usually are  $[OIII]\lambda 5007 / H\beta$  versus  $[NII]\lambda 6584 / H\alpha$ ,  $[OIII]\lambda 5007 / H\beta$  versus  $[SII]\lambda 6717, 6731 / H\alpha$ , and  $[OIII]\lambda 5007 / H\beta$  versus  $[OII]\lambda 6300 / H\alpha$ . The way it works is to mix in the plot hard ionizing emission lines ratio ( $[OIII]\lambda 5007 / H\beta$ ) with low ionization lines ( $[NII]\lambda 6584$ ,  $[SII]\lambda 6717, 6731$ ) known to be present where hydrogen is partially ionized. High  $[NII]\lambda 6584 / H\alpha$ , or  $[SII]\lambda 6717, 6731 / H\alpha$  ratios are usually indicators that the ionization mechanism is more susceptible to be shock and/or AGN than photoionization from hot star UV

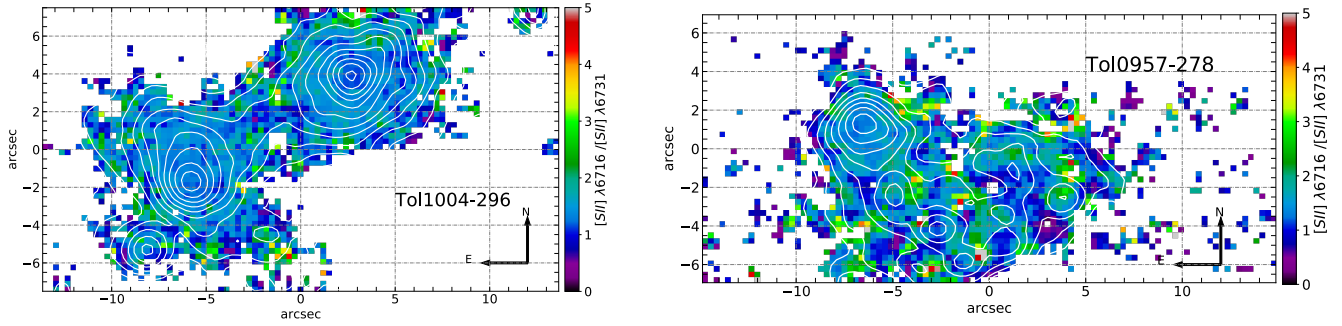


**Figure 5.**  $[\text{SII}]\lambda 6716/[\text{SII}]\lambda 6731$  maps for Tol 1004-296 and Tol 0957-278. For each galaxy,  $\text{H}\alpha$  emission isocontours are presented

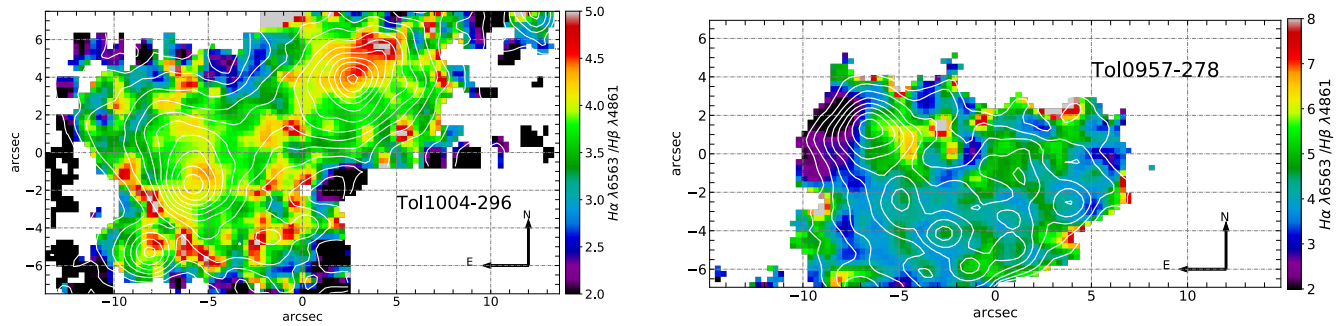


**Figure 6.**  $\text{H}\alpha/\text{H}\beta$  maps for Tol 1004-296 and Tol 0957-278. For each galaxy,  $\text{H}\alpha$  emission isocontours are presented.

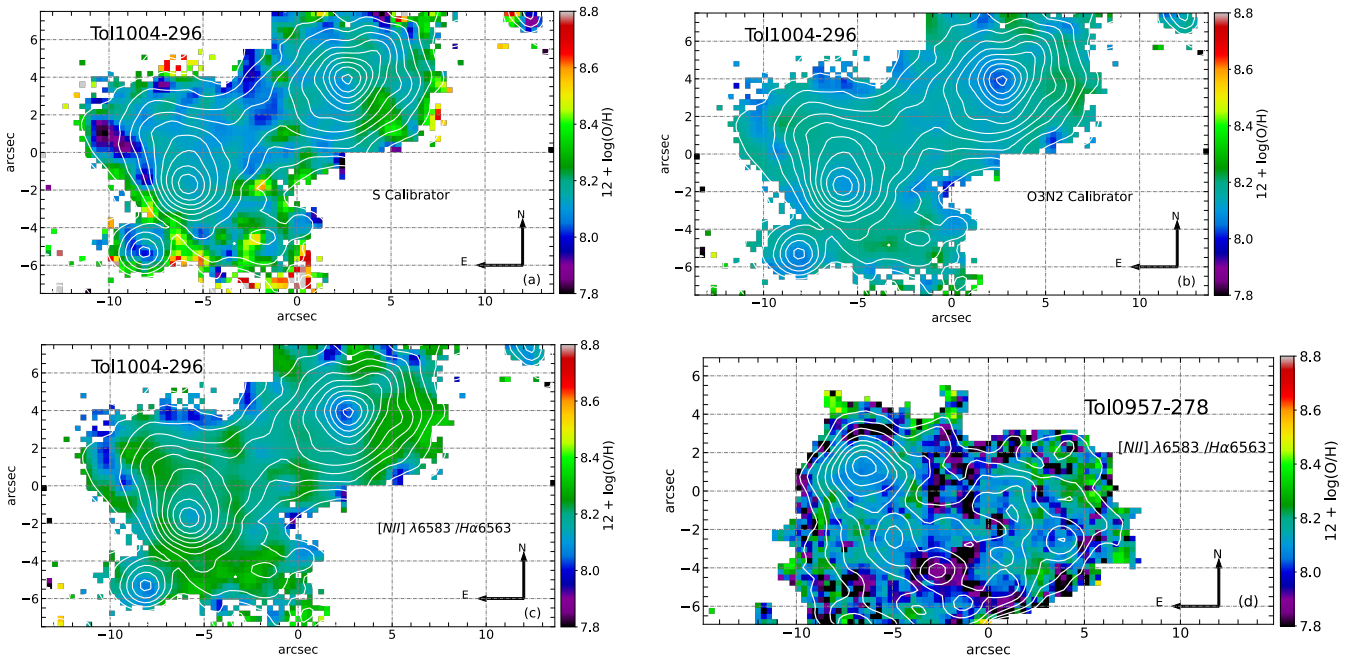


**Figure 7.** Metallicity for Tol 1004-296 and Tol 0957-278. For each galaxy,  $\text{H}\alpha$  emission isocontours are presented. (a): Tol 1004-296 Metallicity map using the *Scalibrator*, (b): Tol 1004-296 Metallicity map using the *O3N2 Calibrator*, (c): Tol 1004-296 Metallicity map using the  $[\text{NII}]\lambda 6583 / \text{H}\alpha$  calibrator, (d): Tol 0957-296 Metallicity map using the  $[\text{NII}]\lambda 6583 / \text{H}\alpha$  calibrator

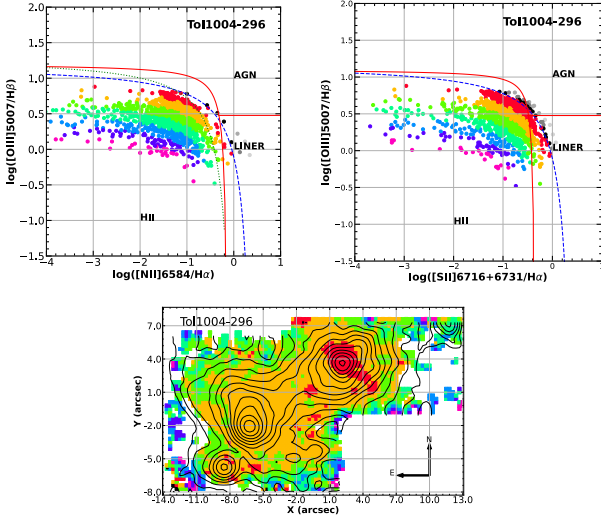


**Figure 8.** BPT diagrams. Color coded represent the distance from the Kewley et al. (2001) (blue dash line) separation. Also shown the Veilleux & Osterbrock (1987) (red lines) and Kauffman et al. (2003) (dotted line) limits  $[OIII]5007/H\beta$  vs  $[NII]6584/H\alpha$  (Upper left),  $[OIII]5007/H\beta$  vs  $[SII]6716+6731/H\alpha$  (Upper right). Spatial locations of the spaxels from the  $[OIII]5007/H\beta$  vs  $[NII]6584/H\alpha$  diagram. The color code is the same as the diagram above (Bottom).

photons. Then the three diagnostic diagrams are divided into three zones: photoionization from hot star UV photons (commonly noted HII regions), AGN, and Shocks (noted as LINER). The diagnostic diagrams, commonly called BPT diagrams, from the name of the authors of Baldwin et al. (1981), are presented in Figure 8, Figure B3, and Figure 9. Except for the MUSE data, we were not able to detect the  $[OI]\lambda 6300$  line, so for data coming from SIFS - SOAR, we only present the first two BPT diagrams.

### 3.5.1 Tol 1004-296

On Figure 8(Top), we can see that, on both plots, as expected, almost all pixels are located on the photoionization by hot stars (HII on the plot). The ratios ranges are  $-4.0 < \log([NII]\lambda 6584/H\alpha) < -0.5$ ,  $-0.5 < \log([OIII]\lambda 5007/H\beta) < -0.8$ , and  $-1.5 < \log([SII]\lambda 6717, 6731/H\alpha) < -0.1$ . Following previous work (Cairós et al. 2017a), we color-code the different points on the plot depending on the distance from the frontier between HII and AGN regions. Both plots also exhibit the different frontiers from Veilleux & Osterbrock (1987); Kewley et al. (2001); Kauffman et al. (2003). The diagram between  $\log([OIII]\lambda 5007/H\beta)$  and  $\log([SII]\lambda 6717, 6731/H\alpha)$  shows that a few points are in the LINER area. The bottom map in Figure 8 shows the spatial distribution of the points in the diagrams (upper panels). The color coding is the same. Red to Violet represent the color of points in the HII zone. The bluer the color, the further from the frontier the point is, from the maximum starburst line. The brightest knot (Knot 1) shows the largest concentration of red points, closer to the maximum starburst line in the diagnostic diagram. Then, around the Knot 1 and Knot 2, the points are orange and correspond to the points a bit further from the frontier.

Figures B3 show both the BPT plots and the spatial distribution map from the MUSE data. Here it was possible to implement the third BPT plot,  $[OIII]\lambda 5007/H\beta$  versus  $[OI]\lambda 6300/H\alpha$ . Two comments can be made when comparing the BTP plots between the

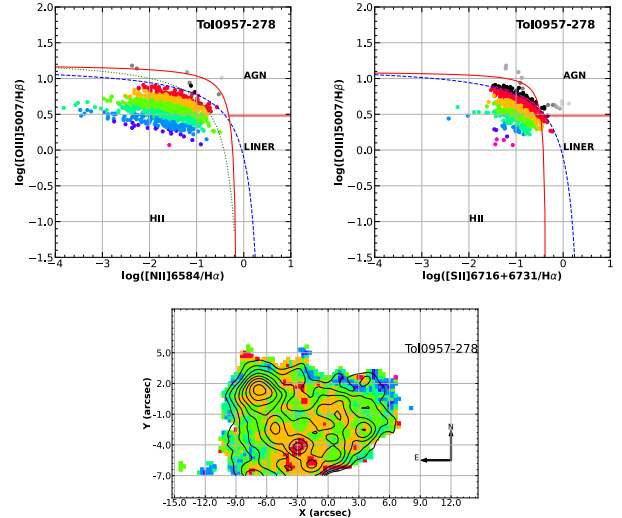


**Figure 9.** Same as Figure 8, but for Tol 0957-278.

data from MUSE and our data. First, as for the SIFS data, almost all points are located in the HII zone, suggesting that what can be seen in the center of the galaxy (with SIFS FoV) is still true for the entire galaxy. Second, we can notice that the ratio is limited to  $-1.5 < \log([OIII]\lambda 5007/H\beta) < +1.0$ . No points are greater than 1.0, when previously, some points had values up to +1.8. It is possible that those points have lower SNR in the outskirts of the SIFS FoV. The ratio  $-3.0 < \log([SII]\lambda 6717, 6731/H\alpha) < +0.1$ , whereas the higher ratio for the SIFS data was -0.1. A few points are located into the LINER zones. The ratio  $-4 < \log([OI]\lambda 6300/H\alpha) < -0.1$  confirms that the overwhelming majority of the ionization mechanism is coming from hot stars UV photons photoionization.

The distribution map in Figure B3 confirms what has been found with the SIFS data in the center. In the outskirts of the galaxy is further from the maximum starburst line.

### 3.5.2 Tol 0957-278

On Figure 9 (Top), both plots show the expected result with pretty much all points located in the HII zone. Line ratios range between  $-4.0 < \log([NII]\lambda 6584/H\alpha) < -0.6$  and between  $+0.2 < \log([OIII]\lambda 5007/H\beta) < +0.8$ . The ratio  $-2.0 < \log([NII]\lambda 6584/H\alpha) < 0.0$  is also showing that most of the pixels are located in the HII area, with only a few points above the Kewley et al. (2001) frontier.

The spatial distribution on Figure 9 also shows that pixels close to the maximum starburst line are concentrated on the bright emission knot 2 and 3.

## 3.6 Advanced kinematical analysis

The other interest of this study is the kinematical analysis aspect. In that regard, we observed both objects using the most resolving grating, M1500M3 available for SIFS. The M1500M3 grating gives a resolution of  $9500@5500\text{\AA}$ <sup>9</sup>. The spectral sampling at  $H\alpha$  is  $0.2877\text{\AA}$  ( $13 \text{ km s}^{-1}$ ). Even with this grating, we also used the data observed with the R700M grating to produce velocity and velocity dispersion maps (not presented here) in order to check our findings.

<sup>9</sup> <https://noirlab.edu/science/programs/ctio/instruments/sifs/characteristics>

In this section, we will describe the velocity and velocity dispersion maps for both galaxies. We also look at the kinematical diagnostic diagrams (Bordalo et al. 2009), applying statistical methods in order to determine possible systematic motions. We will also explore in more detail the line emission profiles in order to describe different degrees of symmetry. As a note, observations done using the M1500M3 grating do not match exactly the fields location showed in Figure 1. Small differences can be noted.

### 3.6.1 Kinematics of Tol 1004-296

Figure 10 shows the radial velocity and the velocity dispersion maps of Tol 1004-296. In both maps, we have superimposed the isocontours from the associated H $\alpha$  emission. The radial velocity ranges from  $1137 \pm 5 \text{ km s}^{-1}$  to  $1205 \pm 6 \text{ km s}^{-1}$ , between the different knots, showing a velocity gradient from the South East to the North West. The velocity amplitude between Knot 1 and Knot 2 is  $25 \pm 4 \text{ km s}^{-1}$  (with Knot 1 being in the blue side). This velocity amplitude does not imply rotation. The velocity field does not show a disk pattern. It can be noticed that, within Knot 1, a small velocity gradient is also present ( $\approx 15 \pm 3 \text{ km s}^{-1}$ ). Knot 3 also shows a small velocity gradient ( $\approx 10 \pm 3 \text{ km s}^{-1}$ ). Also, Knot 5, in between the two larger Knots 1 and 2, shows a low radial velocity of  $1147 \pm 4 \text{ km s}^{-1}$ . Higher radial velocities (from  $1170 \pm 4 \text{ km s}^{-1}$  to  $1180 \pm 4 \text{ km s}^{-1}$ ) can be seen in the South East and South, and the southern tip of Knot 4 shows the highest radial velocity of  $\approx 1200 \pm 6 \text{ km s}^{-1}$ .

The velocity dispersion is also shown in Figure 10. Most of the galaxy shows a supersonic velocity dispersion, with values ranging from  $17 \pm 5 \text{ km s}^{-1}$  to  $34 \pm 2 \text{ km s}^{-1}$  between the different knots. The map shows that the velocity dispersion is not uniform across the galaxy. The centers of emission knots show slightly lower dispersion than the surroundings. This is true for Knot 1, Knot 2, and Knot 3. It is less obvious for Knot 5 and Knot 6. The other important thing to notice is the high velocity dispersion areas. Areas with a velocity dispersion higher than  $40 \pm 5 \text{ km s}^{-1}$  can be found in three locations. First, the area located at  $(-9.0'', +1.0'')$ , the second one is located right between the two main knots with an elongated shape spanning  $\approx 4.2''$ . And finally, an area located at  $(+10.0'', +5.0'')$  also shows velocity dispersion higher than  $45 \pm 7 \text{ km s}^{-1}$ . But, in the last case, because the area is on the outskirts of the galaxy, the SNR is low and the profiles are not very well defined. The region in between the two Knots is the most unexpected with its linear shape. We looked at the data with the R700M grating in order to confirm this unusual shape. The shape, extension, and values are confirmed by those other data. We will come back in more detail on this region when studying the profiles.

Kinematical diagnostic diagrams, pioneered by Muñoz-Tuñón et al. (1996) and Bordalo et al. (2009), offer a robust method for analyzing gas motions in systems lacking disk rotation. These diagrams typically include plots of radial velocity versus emission intensity ( $V_r$  vs.  $Int$ ), velocity dispersion versus emission intensity ( $\sigma$  vs.  $Int$ ), and velocity dispersion versus radial velocity ( $\sigma$  vs.  $V_r$ ). Researchers have demonstrated the utility of these diagrams in studying turbulent motion in HII galaxies (Moiseev & Lozinskaya 2012; Bordalo et al. 2009; Carvalho & Plana 2018) and HII regions (Russeil et al. 2016), enabling the identification of various kinematical features such as expanding shells and relative motion of regions within the object.

To extract information from these diagrams, particularly  $\sigma$  vs.  $Int$  and  $\sigma$  vs.  $V_r$ , we employed a statistical method utilizing the R statistical package (R Development Core Team 2009). Specifically, we utilized the *Mclust* function for model-based clustering, classi-

fication, and probability density estimation based on finite Gaussian mixture modeling (Fraley & Raftery 2007). The Bayesian Information Criterion (BIC) guided the selection of the number of mixture components and the best covariance parameterization. This approach facilitated the identification of independent populations within the diagrams, both in terms of their distribution within the diagrams and their geographical location on the map.

Rather than attempting to separate different components as done in a previous study (Carvalho & Plana 2018), we opted to use the *Density* option, which provides an estimate of the density (probability) for each point on the diagram using a finite mixture model from *Mclust*.

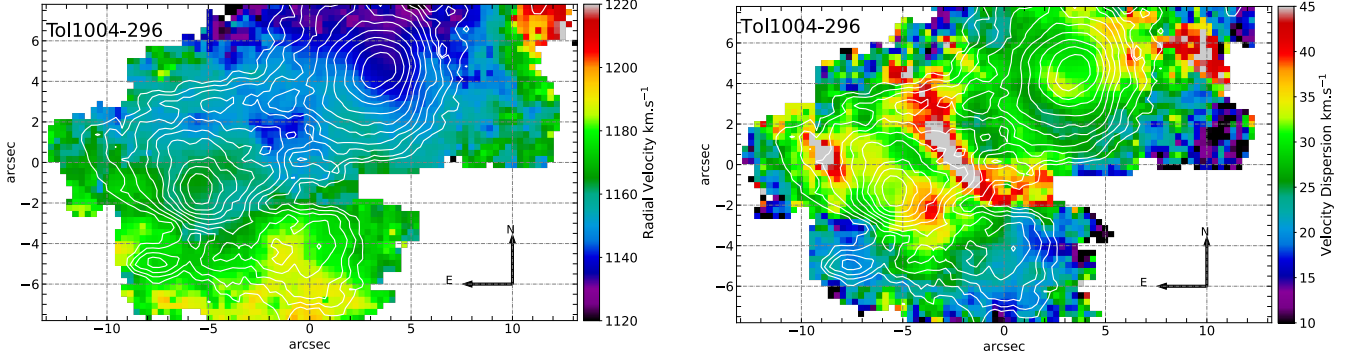
- $\sigma$  vs. Intensity:

Figure 11 comprises three plots. On the left, we present the density map of the velocity dispersion versus intensity diagram, with the density color bar indicating relative values. This map highlights point concentrations with varying colors, with redder shades indicating higher concentration. The middle plot represents the results of a direct analysis with *Mclust* in terms of probability density, identifying five zones of concentration (A1, A2, A3, A4, A5). While some similarities to previous diagrams exist, certain components, such as the inclined bands observed by Moiseev & Lozinskaya (2012), are not as prominent here. Notably, areas A1 and A2 correspond to regions of low turbulence in the interstellar medium (ISM), while A4 resembles the HII region area in previous sketches. The plot on the right attempts to spatially locate the different points from the identified areas (A1, A2, A3, A4, A5) on an spatial location map. Dark grey shading represents A4, corresponding to high-emission areas such as Knot 1 and Knot 2. Areas A1 and A2 encompass peripheral pixels with lower signal-to-noise ratio (SNR), while A3 and A5 surround the two main knots. The A2 area identifies regions with lower velocity dispersion and medium intensity, including Knots 3, 6, and 7. To avoid overloading the map, points that are not in regions A1 to A5 are depicted in light grey. This includes regions with high (above  $35 \text{ km s}^{-1}$ ) and low (below  $18 \text{ km s}^{-1}$ ) velocity dispersion (low velocity dispersion are located on the outskirts of the map).

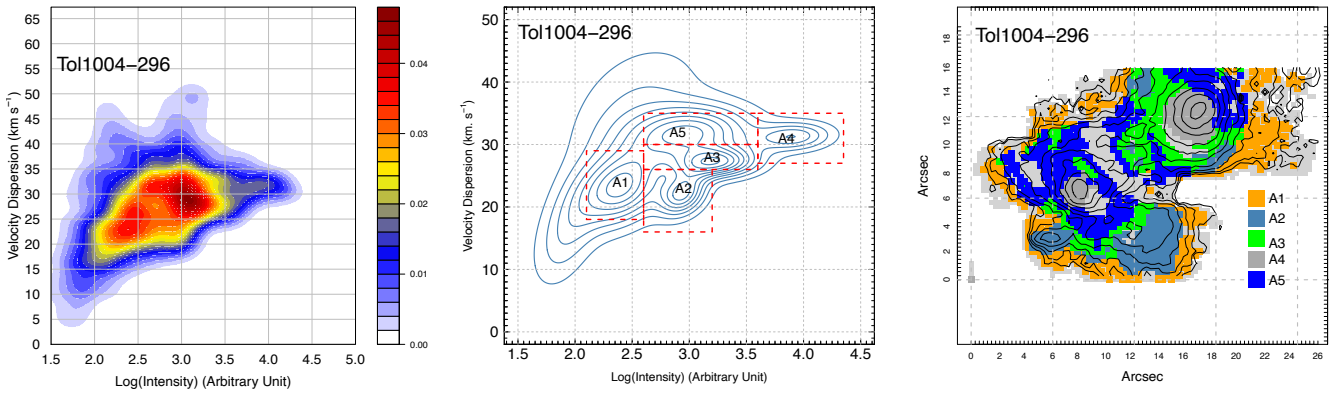
- $\sigma$  vs Radial Velocity:

Figure 12 represents the same plots as before, but for the  $\sigma$  vs Radial Velocity diagram. The left plot shows more clearly the different radial velocity regimes of the galaxy, with the main two concentrated areas representing Knot 1 and Knot 2. This can easily be seen on the velocity map. But the analysis of the probability density, presented in the middle shows that four areas, A1, A2, A3, A4 has been identified by *Mclust*. We decide to include a fifth region, A5, representing the high velocity dispersion area. According to Bordalo et al. (2009), the inclination of different regions in that diagram shows the systemic motion of the region one to the other. We can see that the different zones A1, A2, A3 have systemic motions in one direction. The case of A4 is difficult because the region seems to be vertical. The interpretation of this plot is helped by the next plot on the right. The analysis confirms the assessment we did from the velocity map saying that the Knot 1 shows a velocity gradient (regions A1 and A4 also showing the gradient within Knot 1). The analysis is also showing that the South- South East (Knot 1, Knot 6 and Knot 7) of the galaxy is moving away, but with a low velocity dispersion. The high velocity dispersion area coming from region A5 shows the straight pattern in the middle and area close to Knot 2, confirming the complexity of the dynamic of this Knot.

In conclusion, we can say that this analysis is confirming the analysis that can be done by looking to the different maps, by presenting, in



**Figure 10.** *Left* Radial velocity map. *Right* Velocity dispersion map. We superimposed  $H\alpha$  isocontours on both maps.



**Figure 11.** Kinematical Diagnostic Diagrams. Left:  $\sigma$  vs Intensity diagram using point density visualisation (the density color bar represents relative values normalized to one). Middle:  $\sigma$  vs Intensity diagram after MClust analysis and with five regions identified. Right: Spatial localisation of the pixels inside the five regions.

a more clearer way, the different regimes. It also confirms that, in this kind of galaxies, dynamics is complex and is not dominated by the radial velocity nor the velocity dispersion, since the reconstruction of Figure 12 is a mixture of both.

### 3.6.2 Kinematics of Tol 0957-278

Figure 13 shows the radial velocity and velocity dispersion maps of Tol 0957-278. Radial velocities range between  $1016 \pm 4 \text{ km s}^{-1}$  and  $1041 \pm 5 \text{ km s}^{-1}$ , between the different regions. Unlike Tol 1004-296, the velocity field doesn't exhibit a consistent velocity gradient. However, it's notable that Knot 2 has a lower radial velocity (approximately  $1016 \text{ km s}^{-1} \pm 5 \text{ km s}^{-1}$ ) compared to Knot 1, which has a much higher velocity (approximately  $1041 \pm 5 \text{ km s}^{-1}$ ). Additionally, a small area (located at  $-2''$ ,  $+2.5''$  in Figure 13(Right)), not associated with an emission knot, shows the highest radial velocity (approximately  $1050 \pm 5 \text{ km s}^{-1}$ ).

The velocity dispersion map in Figure 13 reveals non-uniformity, with dispersion values ranging from  $20 \pm 3 \text{ km s}^{-1}$  to  $27 \pm 3 \text{ km s}^{-1}$  between the different regions. Several emission knots (Knots 1, 2, 3, 4, and 5) exhibit lower velocity dispersion in their centers compared to their surroundings. There are some hot spots where the velocity dispersion is between  $35 \pm 3 \text{ km s}^{-1}$  and  $40 \pm 3 \text{ km s}^{-1}$ . One is  $6''$

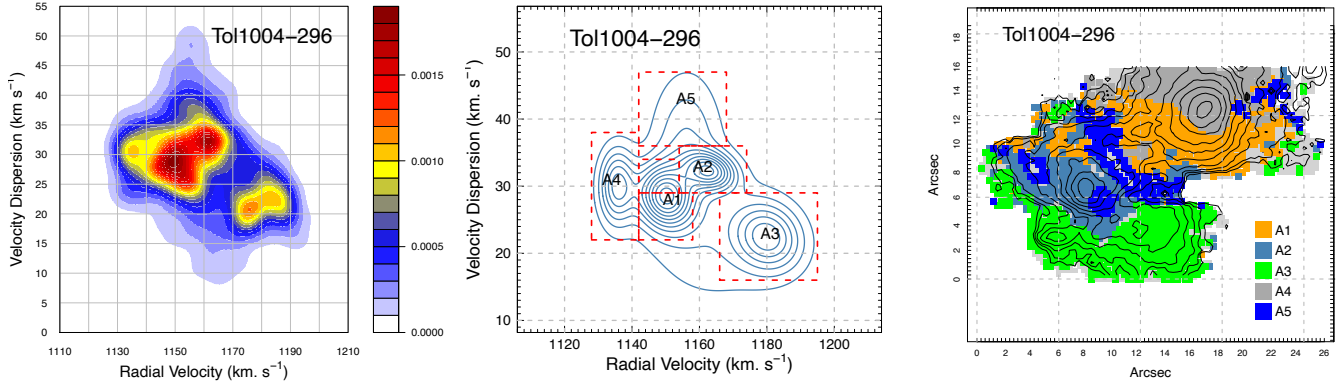
West from Knot 1, another one is  $3''$  North West from Knot 2 and finally one  $6''$  South East from Knot 1.

In the following sections, we present the same statistical analysis as for Tol 1004-296.

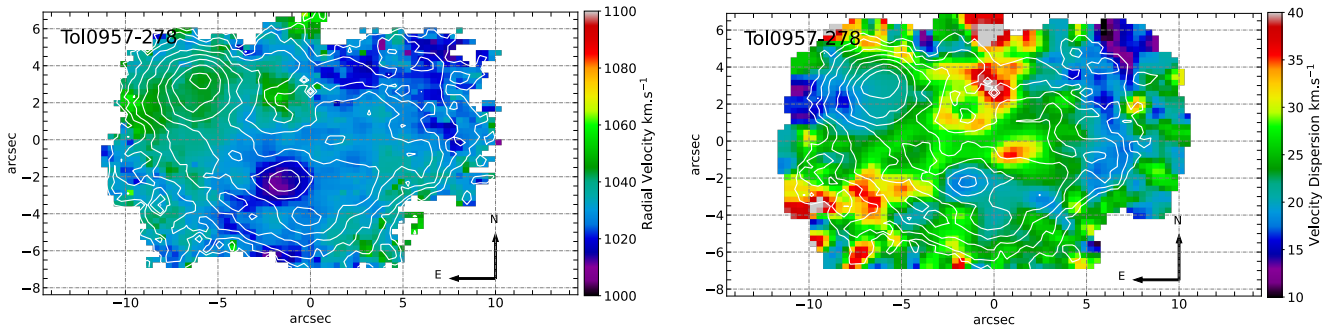
- $\sigma$  vs Intensity:

Figure 14 presents the same three plots as before. On the left is the  $\sigma$  vs Intensity diagram, where the concentration of points is color-coded. The velocity dispersion ranges between approximately  $14 \text{ km s}^{-1}$  and  $40 \text{ km s}^{-1}$ . The overall shape of this plot closely resembles the sketch presented by Moiseev & Lozinskaya (2012), with high-intensity regions exhibiting nearly constant sigma (here approximately  $22 \text{ km s}^{-1}$ ). The area referred to as low turbulence ISM can also be observed, with sigma ranging from approximately  $14 \text{ km s}^{-1}$  to  $40 \text{ km s}^{-1}$  and intensity between 1.7 to 2.5. Finally, a possible inclined band (mentioned as A3 in Figure 14 middle) can be discerned, but we will revisit this later.

The middle plot represents the probability density from the Mclust analysis, identifying three concentration areas: A1, A2, and A3. We add two more regions, A4 representing the high-intensity emission regions, and A5 representing high velocity dispersion and low intensity. The plot on the right depicts the locations of the points from the different areas A1 to A5. The A4 area can be identified with the main emission knots: Knot 1, Knot 2, and Knot 3. A1 represents points on the outskirts of the galaxy. The A5 area, representing high



**Figure 12.** Kinematical Diagnostic Diagrams. Left:  $\sigma$  vs Radial Velocity diagram using point density visualisation (the density color bar represents relative values normalized to one). Middle:  $\sigma$  vs Intensity diagram after MClust analysis and with five regions identified. Right: Spatial localisation of the pixels inside the five regions.



**Figure 13.** Radial velocity map. *Right* Velocity dispersion map. We superimposed H $\alpha$  isocontours on both maps.

velocity dispersion, does not correspond to a particular localization (except perhaps around Knot 8). The location of A3 pixels suggests that it is unlikely to represent an expanding shell as suspected before.

- $\sigma$  vs Radial Velocity:

Figure 15 presents the same three plots as before. On the left is the  $\sigma$  vs Radial Velocity diagram, with the concentration of points color-coded. The MClust result is shown in the middle plot, and no clearly independent regions are present. We only present two areas, A1 and A2, from the probability density analysis. The location of pixels from A1 and A2 is shown in the right plot. A1 represents Knot 1 and the surrounding area, while the A2 area encompasses the region around Knot 2. This analysis is not very informative, as the  $\sigma$  vs Radial Velocity diagram only exhibits two populations, and the analysis does not offer much insight in this case.

### 3.7 Profile Analysis

In this section, we examine the shapes of various H $\alpha$  line profiles across both objects in greater detail. We present 11 profiles from different areas of each galaxy, with each profile representing the sum of a 3x3 pixel region (approximately  $0.9''^2$ ). The objective of this section is to understand the supersonic nature of these objects, particularly whether the very high velocity dispersion (above 30 km

$s^{-1}$ ) is due to the presence of multiple components or is intrinsically large.

#### 3.7.1 Tol 1004-296

Figure 16 displays the H $\alpha$  emission profiles in different areas of Tol 1004-296. The selected areas include regions where the emission is at its maximum (Zones 1, 4, 5, 6, and 11), where the velocity dispersion is highest (Zones 2, 7, 8, 9, and 10), and an area where the velocity dispersion is high but the emission is not at its maximum (Zone 3).

Upon examining the profiles in Zones 1, 4, 5, 6, and 11, it is evident that a single Gaussian adequately fits the emission profile. However, the left wing of Zone 5 is not well-fitted by the Gaussian, suggesting the potential presence of a second component with very low amplitude and velocity. Zones 2 and 3 appear to exhibit the presence of a second component on the low-velocity side.

Zones 7 to 10 encompass the region between the two bright knots (Knot 1 and Knot 2) with a linear shape and higher velocity dispersion. Although these profiles are fairly symmetrical, it is apparent that such broad profiles can be separated into two components. In Figure 16, we attempt such a decomposition for Zones 7 to 10. The results indicate that two components with approximately equal amplitude and sigma can replicate the original profile. However, it is also noticeable that the wings, especially in the low-velocity range, are not well-fitted. Introducing a very low amplitude and low-velocity third

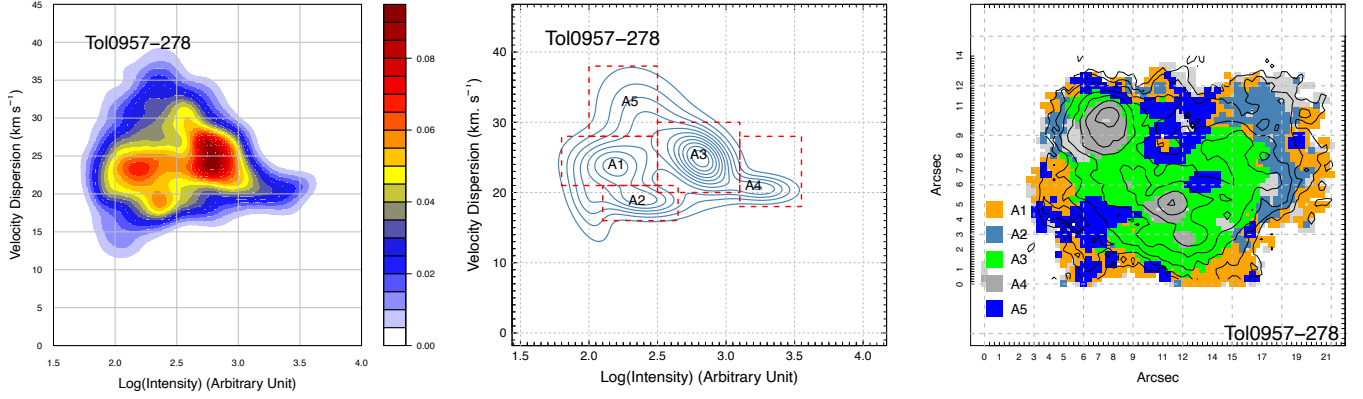


**Figure 14.**  $\sigma$  vs  $Int$  kinematical diagnostic diagrams for Tol 0957-278 (same as Tol 1004-296)

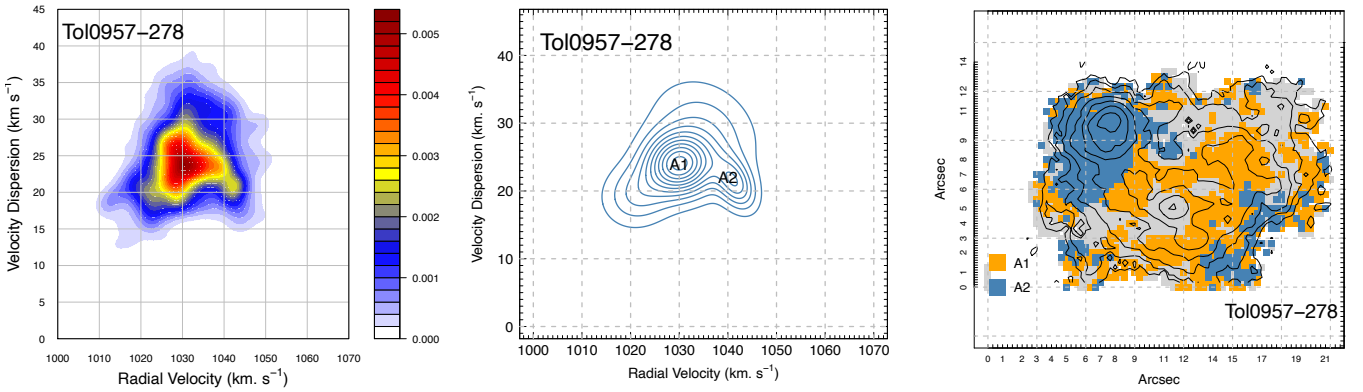


**Figure 15.**  $\sigma$  vs  $V_r$  kinematical diagnostic diagrams for Tol 0957-278 (same as Tol 1004-296)

component may be necessary to accurately reproduce these profiles. However, we refrain from this analysis as a profile can be adequately fitted with numerous components; the crucial aspect is the ability to track these components from profile to profile.

Several observations can be made from this analysis. Firstly, the centers of the different knots can be fitted with only one Gaussian. Secondly, the linear region where the velocity dispersion is highest clearly displays two components (of more or less identical intensities and sigmas) and is indicative of ongoing interactions.

### 3.7.2 Tol 0957-278

Figure 17 presents the  $H\alpha$  emission profiles from different areas of Tol 0957-278. Zones 1, 4, 5, and 6 represent integrated profiles from emission knots, while Zones 2, 7, and 8 display profiles from the surroundings of knots. Zones 3, 9, 10, and 11 correspond to regions with high velocity dispersion.

Profiles from Zones 1, 4, 5, and 6 can be adequately fitted with only one component, as depicted in Figure 17, although Zone 4, Zone 5, and Zone 6 profiles exhibit a low-intensity component on the right wing. Similarly, profiles in Zones 2, 7, and 8 have been fitted with one Gaussian, albeit with a slightly larger velocity dispersion. However, profiles from Zones 3, 9, 10, and 11 display asymmetric shapes and have been fitted with two components, with one having

a higher intensity than the other (but with sigmas remaining more or less the same).

Similar to Tol 1004-296, a low-intensity third component is observed in some profiles. Large profiles from Zones 9 to 11 can be decomposed into two Gaussians, while profiles from low emission areas are primarily fitted with one component.

Additionally, we can note a more pronounced asymmetry with profiles in Zones 9 to 11.

### 3.8 Line ratios and Velocity Dispersion

In this section, we begin to investigate a possible correlation between different line ratios and velocity dispersion, following previous works by Oparin & Moiseev (2018) and D’Agostino et al. (2019). In Figure 18, we present line ratio maps of  $\log([OIII]5007/H\beta)$  and  $\log([SII]/H\alpha)$  for both objects, which are to be compared with the velocity dispersion in Figures 10 and 13.

$[OIII]5007/H\beta$  is sensitive to the radiation field and metallicity, with a high number of high-energy photons producing high ionization, while  $[SII]/H\alpha$  is sensitive to shocks. In the  $\log([OIII]5007/H\beta)$  maps of Tol 1004-296, clear peaks of the ratio are observed in the main emission knots (1, 2, 3, 4, 6, 7), with the ratio diminishing around them. Conversely, the  $[SII]/H\alpha$  ratio shows the exact opposite pattern in the same knots, as expected in regions ionized by massive hot stars. Areas west and northwest from

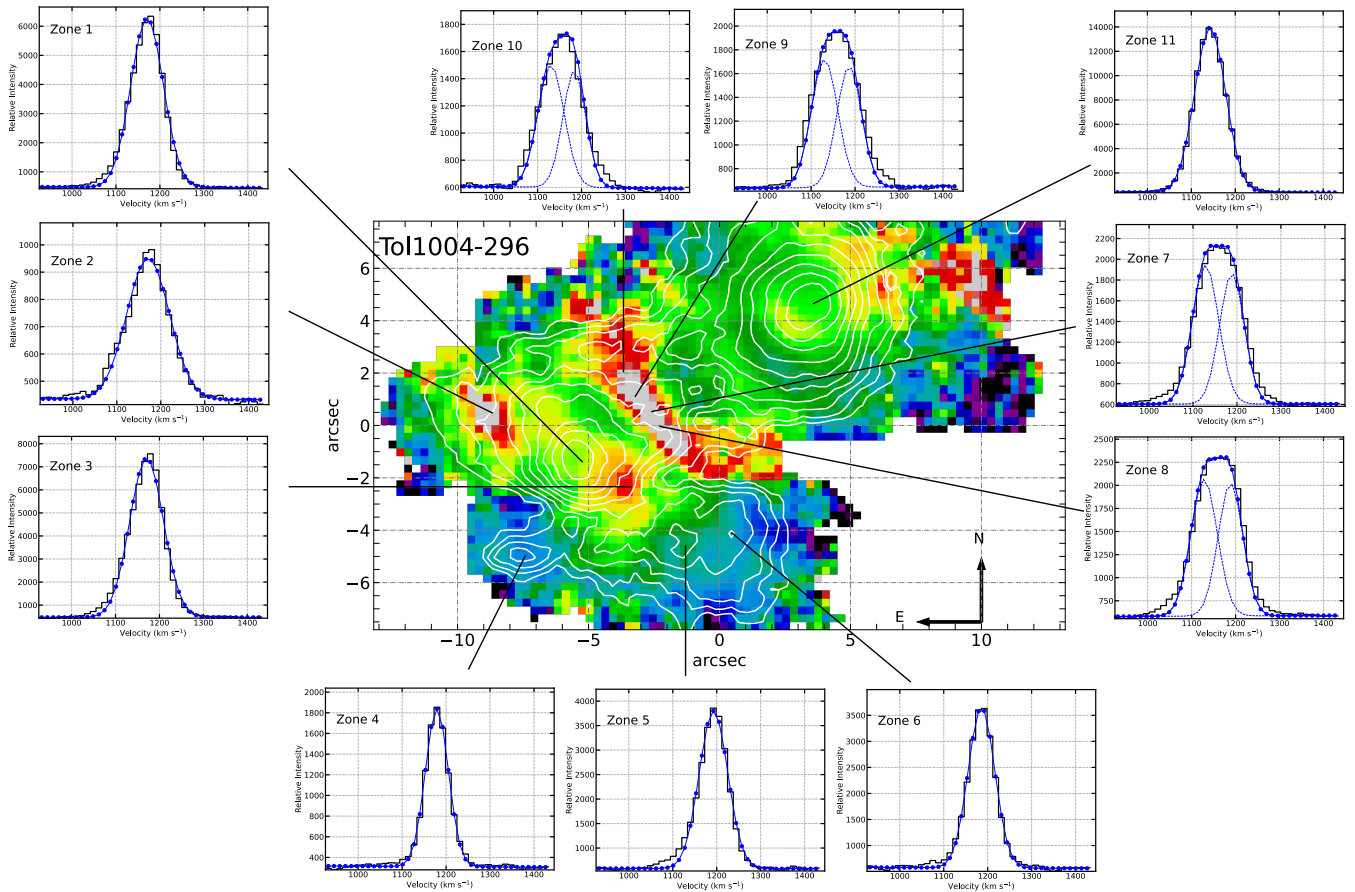


**Figure 16.** Presentation of  $H\alpha$  profiles in different part of Tol 1004-296. Each Zone (1 to 11) represents the integrated profiles in a  $3 \times 3$  pixel box (representing  $\approx 0.9''^2$ ) and represents the intensity versus the radial velocity. Except for Zone 7, Zone 8, Zone 9 and Zone 10, where it was possible to fit two gaussian, the rest of the profiles could be fit with only one gaussian.  $H\alpha$  emission isocontours are superimposed over the velocity dispersion of the galaxy.

Knot 1, as well as an area south of Knot 1, show  $\log([SII]/H\alpha) > -0.3$ , indicating another ionization mechanism, possibly shocks. These maps should also be compared with the velocity dispersion map. Lower velocity dispersions correspond to high values of the  $\log([OIII]5007/H\beta)$  ratio and low values of the  $\log([SII]/H\alpha)$  ratio (located in high emission knots). This correspondence can also be extended to the metallicity map in Figure 7. As mentioned before, metallicity is lower in the star-forming sites. In the area where Tol 1004-296 exhibits a peculiar linear pattern in the velocity dispersion map, the  $\log([OIII]5007/H\beta)$  ratio, though not at its maximum as in Knots 1 and 2, is fairly high, with a value between  $0.58 \pm 0.02$  and  $0.62 \pm 0.02$ . The  $\log([SII]/H\alpha)$  ratio in the same area ranges between  $-0.78 \pm 0.07$  and  $-0.86 \pm 0.05$ , higher compared to the very center of the knots. This linear feature is likely related to the collective mechanical energy from the stellar winds and the supernovae explosions sweeping up the ISM in opposite direction from the center of the two main star-forming knots. The high  $\log([OIII]5007/H\beta)$  and low  $\log([SII]/H\alpha)$  is characteristic of star-forming regions of Tol 0957-278. For the Knot 2, the ionization level, as given by  $\log([OIII]5007/H\beta)$ , is high compared to Knot 1. Combining this information with the low oxygen abundance observed in Knot 2, one may conclude that there must have been a recent inflow of metal-poor gas to this region feeding the ongoing star formation. This is also in agreement with the low velocity dispersion in the star forming knots.

#### 4 CONCLUSIONS

In this work, we present IFU observations of two  $HII$  galaxies, Tol 1004-296 and Tol 0957-278. The lower spectral resolution observations allow us to produce several main emission line monochromatic maps, along with electron density, reddening, line ratios, and metallicity maps. We also had the possibility to explore the ionization mechanism using BPT diagrams. Higher spectral resolution data enable the generation of precise radial velocity and velocity dispersion maps.

In this work, we delved deeper into the analysis of the kinematics by using kinematical diagnostic diagrams to show if systemic motions, expanding shells were present in these two objects and how this can help to understand the characteristics of the ISM.

Both galaxies show the common features we expect for  $HII$  galaxies. They present several bright emissions peaks in the different lines. We count seven and eight knots, respectively, for Tol 1004-296 and Tol 0957-278. Extinction, due to dust lane, can be severe, as in Knot 1 in Tol 0957-278. The metallicity does not exceed 8.5, and the ionization mechanism is dominated by photoionization from OB stars.

The kinematical perspective confirms the image we usually have of such objects: no disk rotation, but a slight velocity gradient is present between the two main knots in the Tol 1004-296 case. However, the velocity dispersion shows its importance when we applied a more in-depth analysis using statistical tools to analyze the diagnostics

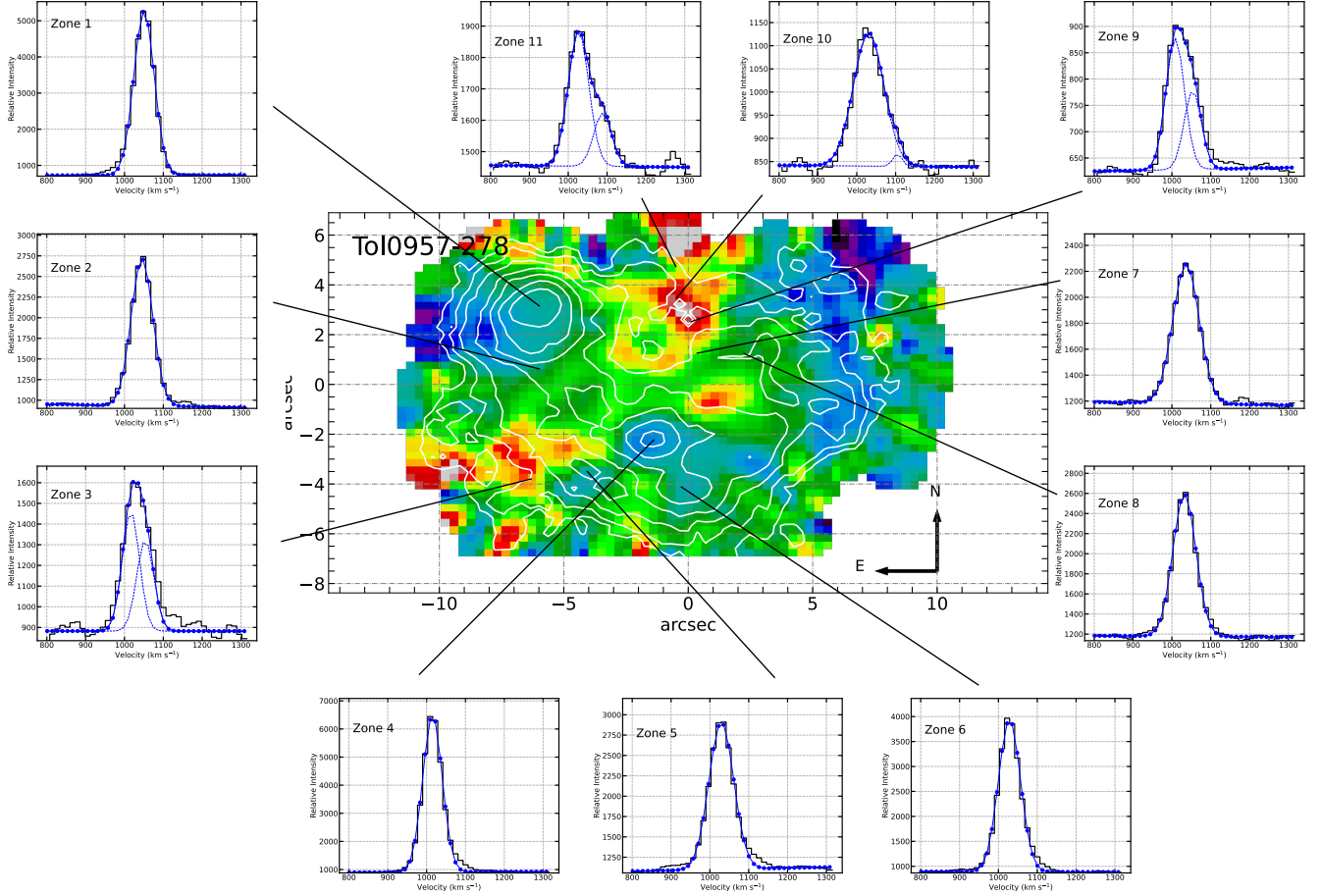


**Figure 17.** Same as Tol 1004-296. Here Zone 3, Zone 9, Zone 10 and Zone 11 profiles, have been fitted with two gaussian. Contrary to Tol 1004-296, there is a high and low amplitude gaussian.

diagrams. We didn't find expanding shells, but systemic motions are present with signatures of turbulence. The profile analysis of the  $H\alpha$  line profile shows that emission is made of one component where the emission peaked and of two components in some specific areas, where the velocity dispersion is higher, showing possible turbulent motions there.

We can categorize the results of this study into two main findings.

Firstly, we confirm a correlation observed in previous studies (see Table 5), wherein a peak of emission corresponds to low velocity dispersion. This result can be extended to  $[OIII]5007/H\beta$ ,  $[SII]/H\alpha$  line ratios maps, and metallicity maps. We found that peak emission regions (knots) correspond to maximum  $[OIII]5007/H\beta$  ratio, minimum  $[SII]/H\alpha$  ratio. Additionally empirical metallicity maps revealed lower metallicity in regions with low velocity dispersion. In Tol 1004-296, we verified this using three different calibrators, albeit with slightly different values. Similarly, in Tol 0957-278, the metallicity map reflects lower values where the velocity dispersion is low. It has to be noted that these correspondences are present in almost all previous studies (see Table 5). Authors of these studies mentioned the correspondence between peak emission with peak  $[OIII]5007/H\beta$  ratio, low  $[SII]/H\alpha$ , and sometimes with low metallicity, but, to our knowledge, none of these studies have connected this with a low velocity dispersion. We summarize these findings in Table 5, which lists 16 objects (including this study) exhibiting such characteristics.

Secondly, we note a significant result regarding the velocity dispersion map of Tol 1004-296. Figure 10 clearly depicts a linear region with high velocity dispersion ( $\approx 50 \pm 5 \text{ km s}^{-1}$ ) situated between the brighter emission knots, a feature also observed in data obtained from the R700M grating. The decomposition of these profiles in Figure 16, albeit crude, reveals two distinct Gaussians. Notably, we did not encounter a similar feature in the literature's velocity dispersion maps. While we lack a definitive interpretation or explanation for this phenomenon, one possible explanation is the collision of material pushed from both Knot 1 and Knot 2, leading to the formation of a region with high velocity dispersion.

Results regarding the different line ratios in the knots are consistent with the image of young massive star formation sites, with high  $[OIII]5007/H\beta$  ratio, low  $[SII]/H\alpha$  ratio and low metallicity. The fact that the velocity dispersion is also lower in these areas compared to the surroundings, tend to show that turbulent motions are propagated around the area where the emission is at its maximum. This seems to be corroborated by the  $[SII]/H\alpha$  ratio, sensitive to shocks.

## ACKNOWLEDGEMENTS

Based on observations obtained at the Southern Astrophysical Research (SOAR) telescope, which is a joint project of the Ministério da

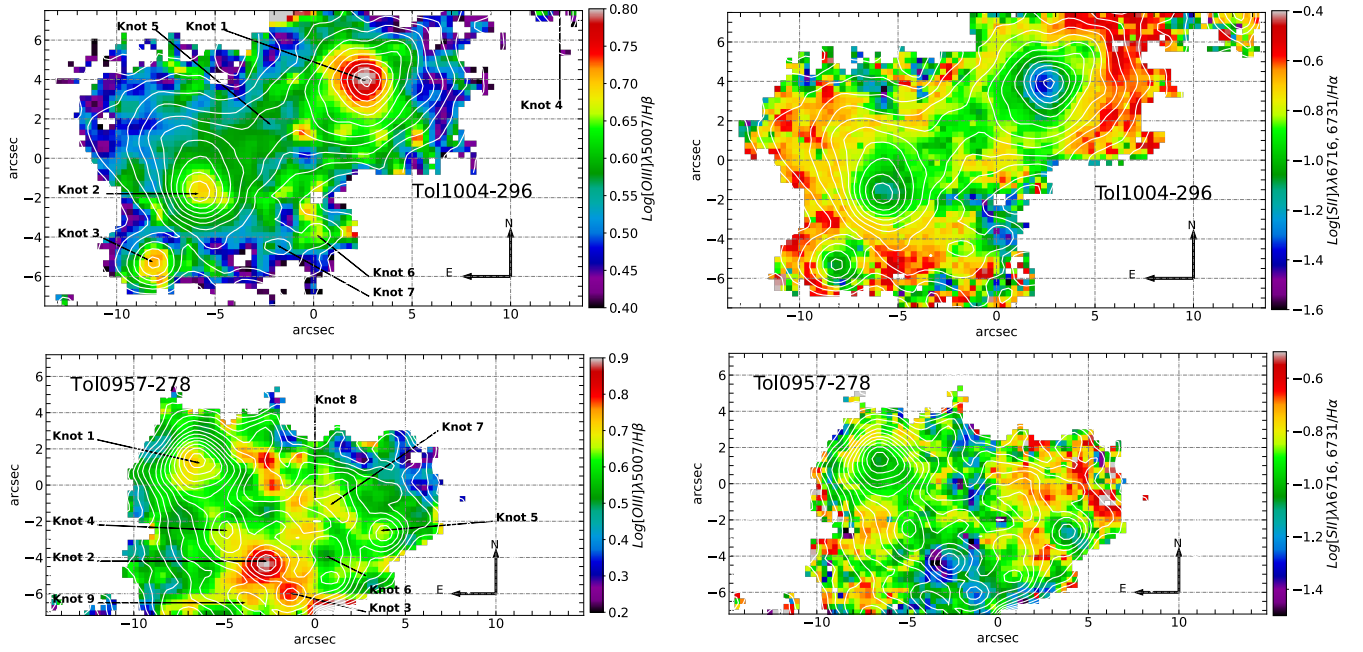


**Figure 18.** First row Tol 1004-296- Left:  $\log([OIII]5007/H\beta)$  line ratio. Right:  $\log([SII]/H\alpha)$  line ratio. Isocontours represent  $H\alpha$  emission. Second row Tol 0957-278- Left:  $\log([OIII]5007/H\beta)$  line ratio. Right:  $\log([SII]/H\alpha)$  line ratio. Isocontours represent  $H\alpha$  emission.

**Table 5.** Summary of key galaxies characteristics of a sample of BCGs: (1) This work; (2) Cairós et al. (2015); (3) Cairós et al. (2020); (4) Cairós et al. (2022); (5) Egorov et al. (2021); (6) Castillo-Morales et al. (2011); (7)García-Lorenzo et al. (2008)

Galaxy	High emission. vs Low $\sigma$	High emission vs Low Metallicity	Low Metallicity vs Low $\sigma$	Velocity Gradient	Rotating Disk
Tol 1004-296 <sup>(1)</sup>	Yes	Yes	Yes	Yes	No
Tol 0957-278 <sup>(1)</sup>	Yes	Yes	Yes	Yes	No
Haro 11 <sup>(2)</sup>	Yes	Yes	Yes	No	No
Haro 14 <sup>(2,4)</sup>	Yes	Yes	Yes	No	No
Tol 0127-397 <sup>(2)</sup>	Yes	Yes	Yes	Yes	No
Tol 1924-416 <sup>(2)</sup>	Yes	Yes	Yes	No	No
Tol 1937-423 <sup>(2)</sup>	Yes	Yes	Yes	Yes	Yes
Mrk 900 <sup>(2,3)</sup>	Yes	Yes	Yes	Yes	No
Mrk 1131 <sup>(2)</sup>	Yes	Yes	Yes	Yes	Yes
DDO 53 <sup>(5)</sup>	Yes	Yes	Yes	No	No
NGC 7673 <sup>(6)</sup>	-( $\alpha$ )	Yes	Yes	-	-
Mrk 370 <sup>(7)</sup>	Yes	Yes	Yes	Yes	No
Mrk 35 <sup>(7)</sup>	Yes	Yes	Yes	Yes	No
Mrk 297 <sup>(7)</sup>	Yes	Yes	Yes	No	No
Mrk 314 <sup>(7)</sup>	Yes	Yes	Yes	No	No
III Zw 102 <sup>(7)</sup>	Yes	Yes	Yes	Yes	No

( $\alpha$ ) no dispersion map available

Ciência, Tecnologia, e Inovação (MCTI) da República Federativa do Brasil, the U.S. National Optical Astronomy Observatory (NOAO), the University of North Carolina at Chapel Hill (UNC), and Michigan State University (MSU). We thank LNA staff for his support during the runs and for data reduction. We acknowledge the usage of the Nasa Extragalactic Database (<http://ned.ipac.caltech.edu/>) and R free software. The authors also thank J.C. Lambert (LAM) for the help provided in the creation of certain figures. HP thanks the Laboratoire d’Astrophysique de Marseille (LAM) and Aix Marseille Université (AMU) for the financial support during his staying at LAM in December 2023. VGA thanks Fundação de Amparo e Pesquisa do Estado da

Bahia (FAPESB) for the financial under fellowship BOL0345/2021. Authors would like to thank the referee for their helpful remarks

## DATA AVAILABILITY

The data underlying this article will available in the NOIRLab Astro Data Archive (<https://astroarchive.noirlab.edu/>) or upon request to the authors.

## REFERENCES

- Alloin, D., Collin-Souffrin, S., Joly, M., Vigroux, L. 1979, *â*, 78, 200  
 Ambartsumian, V.A. 1968, *L’Astronomie*, Vol. 82, p.101  
 Amram, P. 1991, Thesis, Université de Provence: Cinématique du gaz ionisé dans les galaxies spirales. Effets de l’environnement dans les galaxies binaires et dans les amas  
 Bacon, R., Accardo, M., Adjali, L., Anwand, H., Bauer, S., Biswas, I., Blaizot, J. et al. 2010, *Proceedings of the SPIE*, Volume 7735, id. 773508  
 Baldwin, J. A., Phillips, M. M., Terlevich, R. 1981, *PASP*, 93, 5  
 Bergvall, N., Olofsson, K., 1986., *A&AS*, 64, 469  
 Bordalo, V., Plana, H., Telles, E., 2009, *ApJ*, 696, 1668  
 Bordalo, V., Telles, E., 2011 *ApJ*, 735, 52  
 Brennan, R., Pandya, V., Somerville, R.S., Barro, G., Bluck, A.F.L., Taylor, E.N., Wuys, S., Bell, E.F., Dekel, A., Faber, S. et al. 2017, *MNRAS*, 465, 619  
 Buckalew, B.A., Koblunicky, H.A., Dufour, R.J., 2005, *ApJS*, 157, 30  
 Calzetti, D., Kinney, A.L., Storchi-Bergmann, T., 1994, *ApJ*, 429, 582  
 Calzetti, D., Armus, L., Bohlin, R.C., Kinney, A.L., Koornneef, J., Storchi-Bergmann, T., 2000, *ApJ*, 533, 682  
 Campbell, A. 1988, *ApJ*, 335, 644  
 Carvalho, M.S., Plana, H., 2018, *MNRAS*, 481, 122  
 Castillo-Morales, A., Gallego, J., Pérez-Gallego, J., Guzmán, R., Muñoz-Mateos, J.C., Zamorano, J., Sánchez, S.F., 2011, *MNRAS*, 411, 1819  
 Cairós, L.M., García-Lorenzo, B., Caon, N., Vílchez, J.M., Papaderos, P., Noeske, K., 2003, *Ap&SS*, 284, 611

- Cairós, L.M., Caon, N., Weibacher, P.M., 2015, *A&A*, 577, A21  
 Cairós, L.M., González-Pérez, J.N., 2017, *A&A*, 600, A125  
 Cairós, L.M., González-Pérez, J.N., 2017, *A&A*, 608, A119  
 Cairós, L.M., González-Pérez, J.N., 2020, *A&A*, 634, A95  
 Cairós, L.M., Caon, N., Weibacher, P.M., Manso Sainz, R., 2022, *A&A*, 164, A144  
 Chandar, R., Leitherer, C., Tremonti, C.A., 2004, *ApJ*, 604, 153  
 Chhatkuli, Daya Nidhi, Paudel, Sanjaya, Bachchan, Rajesh Kumar, Aryal, Binil, Yoo, Jaewon, 2023, *MNRAS*, 520, 4953  
 Conti P.S. and Morris P.W. 1990 *AJ*99, 898  
 Cresci, G., Vanzi, L., Sauvage, M., Santangelo, G., van der Werf, P., 2010, *A&A*, 520, A82  
 Cuisinier, F., Westera, P., Telles, E., Buser, R., 2006, *A&A*, 455, 825  
 D'Agostino, J.J., Kewley, L.J., Groves, B.A., Medling, A., Dopita, M.A., Thomas, A.D., 2019, *MNRAS*, 485, L38  
 Denicoló, G., Terlevich, R., Terlevich, E., 2002, *MNRAS*, 330, 69  
 Dinerstein, H.L., in *The interstellar medium in galaxies*; Proceedings of the 2nd Teton Conference, Dordrecht, Netherlands, Kluwer Academic Publishers, 1990, p. 257-285.  
 Domínguez, A., Siana, B.; Henry, A.L., Scarlata, C., Bedregal, A.G., Malkan, M., Atek, H., Ross, N.R. et al. 2013, *ApJ*, 763, 145  
 Dopita, M.A., Groves, B.A., Sutherland, R.S., Kewley, L.J., 2003, *ApJ*, 583, 727  
 Doublier, V., Caulet, A., Comte, G., 1999, *A&AS*, 138, 213  
 Egorov, O.V., Lozinskaya, T.A., Vasiliev, K.I., Yarovova, A.D., Gerasimov, I.S., Kreckel, K., Moiseev, A.V., 2021, *MNRAS*, 508, 2650  
 Eisenhauer, F., Abuter, R., Bickert, K., Biancat-Marchet, F., Bonnet, H., Brynnel, J., Conzelmann, R.D., Delabre, B. et al. 2003, *SPIE*, 4841, 1548E  
 Engelbracht, C.W., Rieke, G.H., Gordon, K.D., Smith, J.D.T., Werner, M.W., Moustakas, J., Willmer, C.N.A., Vanzi, L., 2008, *ApJ*, 678, 804  
 Fraga, L., Overall status and results from the commissioning and early science of SIFS. [s.n.], 2018, [www.soar-telescope.org/soar/sites/default/files/SIFS/Fraga\\_GMT2018.pdf](http://www.soar-telescope.org/soar/sites/default/files/SIFS/Fraga_GMT2018.pdf)  
 Fraley, C., Raftery, A.E., 2007, *Journal of Statistical Software*, v. 18, issue 6  
 García-Lorenzo, B.; Cairós, L.M., Caon, N.; Monreal-Ibero, A.; Kehrig, C., 2008, *ApJ*, 677, 201  
 Gil de Paz, A., Madore, B.F., Pevunova, O., 2003, *ApJS*, 147, 29  
 Gil de Paz, A., Madore, B.F., 2005, *ApJS*, 156, 345  
 Greis, S.M.L., Stanway, E.R., Davies, L.J.M., Levan, A.J., 2016, *MNRAS*, 459, 2591  
 Hamuy, M.; Walker, A.R., Suntzeff, N.B., Gigoux, P., Heathcote, S.R., Phillips, M.M., 1992, *PASP*, 104, 533  
 Haro, G., 1956, *AJ*, 61, 178  
 Hunter, D.A., Elmegreen, B.G., 2004, *AJ*, 128, 2170  
 Kauffmann, G., Heckman, T.M., Tremonti, C., Brinchmann, J., Charlot, S., White, S.D.M., Ridgway, S.E., Brinkmann, J., Fukugita, M., Hall, P.B., 2003, *MNRAS*, 346, 1055  
 Kehrig, C., Telles, E., Cuisinier, F., 2004, *AJ*, 128, 1141  
 Kewley, L.J., Dopita, M.A., Sutherland, R.S., Heisler, C.A., Trevena, J., 2001, *ApJ*, 556, 121  
 Kim, J., Chung, A., Wong, O.I., Lee, B., Sung, E., Staveley-Smith, L., 2017, *A&A*, 605, A54  
 Kunth, D., Joubert, M., 1985, *A&A*, 142, 411  
 Kunth, D., Maurogordato, S., Vigroux, L., 1988, *A&A*, 204, 10  
 Kunth, D., Östlin, G., 2000, *A&ARv*, 10, 1  
 Lagos, P., Telles, E., Melnick, J., 2007, *A&A*, 476, 89  
 Lagos, P., Telles, E., Muñoz-Tuñón, C., Carrasco, E.R., Cuisinier, F., Tenorio-Tagle, G., 2009, *AJ*, 137, 5068  
 Lagos, P., Telles, E., Nigoche-Netro, A., Carrasco, E.R., 2011, *AJ*, 142, 162  
 Lepine, J.R.D., de Oliveira, A.C., Figueredo, M.V., Castilho, B.V., Gneiding, C., Barbuy, B. et al. 2003, *SPIE*, 4841, 1086  
 Luridiana, V., Morisset, C., Shaw, R.A., 2015, *A&A*, 573, A42  
 Mac Low, M.-M., Ferrara, A., 1999, *ApJ*, 513, 142  
 McCall, M.L., Rybski, P.M., Shields, G.A., 1985, *ApJS*, 57, 1  
 Masegosa, J., Moles, M., Campos-Aguilar, A., 1994, *ApJ*, 420, 576  
 Marino, R.A., Rosales-Ortega, F.F., Sánchez, S.F., Gil de Paz, A., Vílchez, J., Miralles-Caballero, D., Kehrig, C., Pérez-Montero et al. 2013, *A&A*, 559, 114  
 Markarian, B.E., 1967, *Astrofizika*, 3, 24  
 Méndez, D.I., Esteban, C., 2000, *A&A*, 359, 493  
 Moiseev, A.V., Lozinskaya, T.A., 2012 *MNRAS*, 423, 1831  
 Muñoz-Tuñón, C., Tenorio-Tagle, G., Castañeda, H.O., Terlevich, R., 1996, *AJ*, 112, 1636  
 Muñoz-Mateos, J.C., Gil de Paz, A., Zamorano, J., Boissier, S., Dale, D. A., Pérez-González, P.G., Gallego, J., Madore et al. 2009, *ApJ*, 703, 1569  
 Oparin, D.V., Moiseev, A.V., 2018, *Astrophysical Bulletin*, Vol. 73, Issue 3, p298  
 Osterbrock, D.E., Ferland, G.J., 2006, *Astrophysics of gaseous nebulae and active galactic nuclei*, 2nd. ed. by D.E. Osterbrock and G.J. Ferland. Sausalito, CA: University Science Books,  
 Papaderos, P., Loose, H.-H., Thuan, T.X., Fricke, K.J., 1996, *A&AS*, 120, 207  
 Papaderos, P., Loose, H.-H., Fricke, K.J., Thuan, T.X., 1996, *A&A*, 314, 59  
 Papaderos, P., Izotov, Y.I., Thuan, T.X., Noeske, K.G., Fricke, K.J., Guseva, N.G., Green, R.F., 2002, *A&A*, 393, 421  
 Paturel, G., Theureau, G., Bottinelli, L., Gougenheim, L., Courdreau-Durand, N., Hallet, N., Petit, C. 2003, *A&A*, 412, 57  
 Penston, M.V., Fosbury, R.A., Ward, M., Wilson, A., 1977, *MNRAS*, 180, 19  
 Perret, V., Renaud, F., Epinat, B., Amram, P., Bournaud, F., Contini, T., Teyssier, R., Lambert, J.C., *A&A*, 562, 1  
 Pustilnik, S.A., Martin, J.-M. 2007, *A&A*, 464, 859  
 Pilyugin, L.S., Grebel, E.K., Mattsson, L., 2012, *MNRAS*, 424, 2316  
 Pilyugin, L.S., Grebel, E.K., 2016, *MNRAS*, 457, 3678  
 Reif, K., Mebold, U., Goss, W.M., van Woerden, H., Siegman, B., 1982, *A&AS*, 50, 451  
 Rybicki, G.B., Lightman, A.P., *Radiative Processes in Astrophysics*, 2004, Ed. WILEY-VCH Verlag GmbH & Co. KGaA.  
 D. Russeil, J. Tigé, C. Adami, L.D. Anderson, N. Schneider, A. Zavagno, M.R. Samal, P. Amram, et al., 2016, *A&A*, 587, A135  
 Salzer, J.J., MacAlpine, G.M., Boroson, T.A., 1989, *ApJS*, 70, 447  
 Salzer, J.J., MacAlpine, G.M., Boroson, T.A., 1989, *ApJS*, 70, 479  
 Sargent, W.L.W., Searle, L., 1970, *ApJ*, 162, L155  
 Schaerer, D., Contini, T., Pindao, M., 1999, *A&AS*, 136, 35  
 Schwartz, C.M., Martin, C.L., Chandar, R., Leitherer, C., Heckman, T.M., Oey, M.S., 2006, *ApJ*, 646, 858  
 Shaw, R.A., Dufour, R.J., 1995, *PASP*, 107, 896  
 Smith, M.G., 1975, *ApJ*, 202, 591  
 Smith, M.G., Aguirre, C., Zemelman, M., 1976, *ApJS*, 32, 217S  
 Stevens, I.R., Forbes, D.A., Norris, R.P., 2002, *MNRAS*, 335, 1079  
 Sung, E.C., Chun, M.S., Freeman, K. C., Chaboyer, B., in *The Dynamics, Structure & History of Galaxies: A Workshop in Honour of Professor Ken Freeman*. ASP Conference Proceedings, Vol. 273, 2002, p.341  
 Telles, E., Terlevich, R., 1995, *MNRAS*, 275, 1  
 Telles, E., Terlevich, R., 1997, *MNRAS*, 286, 183  
 Telles, E., Melnick, J., Terlevich, R., 1997, *MNRAS*, 288, 78  
 Terlevich, R., Melnick, J., Masegosa, J., Moles, M., Copetti, M.V.F., 1991, *A&AS*, 91, 285  
 Terlevich, R., Melnick, J., 1981, *MNRAS*, 195, 839  
 Tody, D. 1986, *SPIE*, 627, 733  
 Thuan, T.X., Martin, G.E., 1981, *ApJ*, 247, 823  
 Thuan, T.X., 1983, *ApJ*, 268, 667  
 Thuan, T.X. 1985, *ApJ*, 299, 881  
 Torres-Campos, A., Terlevich, E., Rosa-González, D., Terlevich, R., Telles, E., Díaz, A.I., 2017, *MNRAS*, 471, 2829  
 Vacca, W.D., Conti, P.S., 1992, *ApJ*, 401, 543  
 Vanzi, L., Cresci, G., Sauvage, M., Thompson, R., 2011, *A&A*, 534, A70  
 Veilleux, S., Osterbrock, D.E., 1987, *ApJS*, 63, 295  
 Westera, P., Cuisinier, F., Telles, E., Kehrig, C., 2004, *MNRAS*, 423, 133  
 Zhang, Hong-Xin, Smith, R., Oh, Se-Heon, Paudel, S., Duc, P.A., Boselli, A., Côté, P., Ferrarese, L., et al. 2020, *ApJ*, 900, 152  
 Zwicky, I.F., 1964, *ApJ*, 140, 1467  
 Zwicky, I.F., 1966, *ApJ*, 143, 192  
 Zwicky, F., Zwicky, M.A., 1971, *Guemligen: Zwicky, |c1971*

**APPENDIX A: HISTOGRAMS OF DIFFERENT PARAMETERS:  $[\text{SII}]\lambda 6716/[\text{SII}]\lambda 6731$ ,  $\text{EW}(\text{H}\beta)$ ,  $\text{E}(\text{B}-\text{V})$  AND DIAGNOSTICS DIAGRAMS LINE RATIOS**

**APPENDIX B: TOL 1004-296 MUSE DATA**

**B1 Monochromatic Maps**

**B2 Lines Diagnostics maps**

**B3 Ionization mechanisms diagrams and Velocity map**

This paper has been typeset from a  $\text{T}_{\text{E}}\text{X}/\text{L}_{\text{A}}\text{T}_{\text{E}}\text{X}$  file prepared by the author.

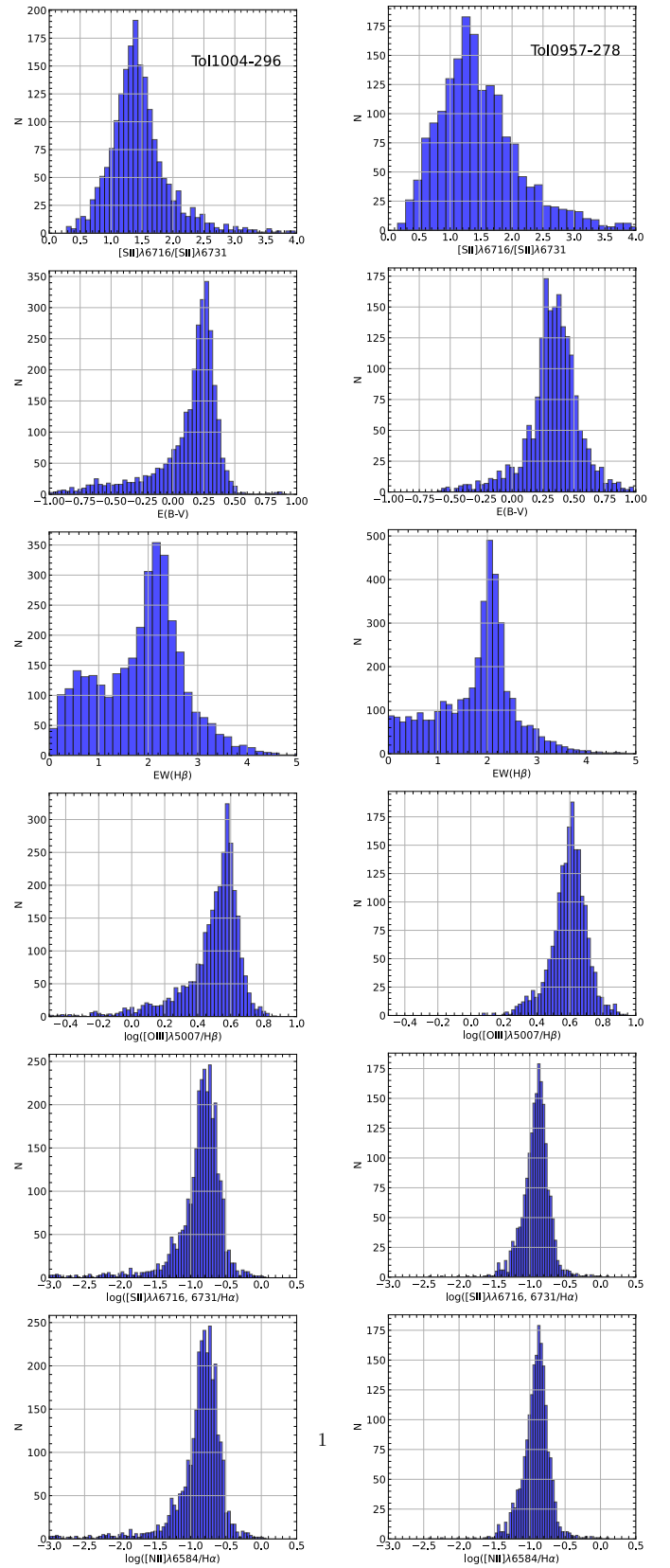


**Figure A1.** Histograms representing different parameters:  $[\text{SII}]\lambda 6716/[\text{SII}]\lambda 6731$ ,  $\text{EW}(\text{H}\beta)$ ,  $\text{E}(\text{B}-\text{V})$  and diagnostics diagrams line ratios for both galaxies, left column for Tol 1004-296 and right column for Tol 0957-278

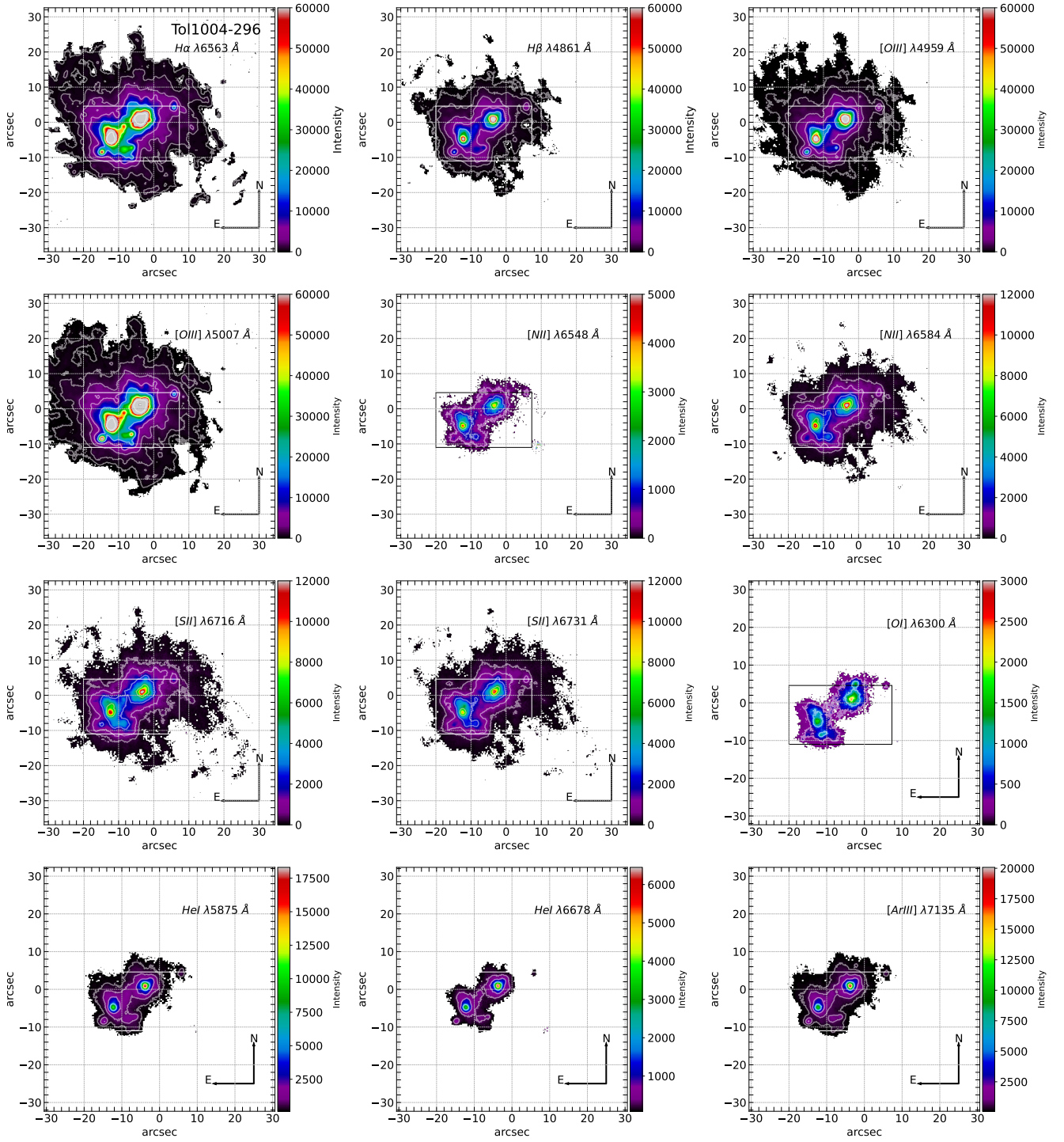
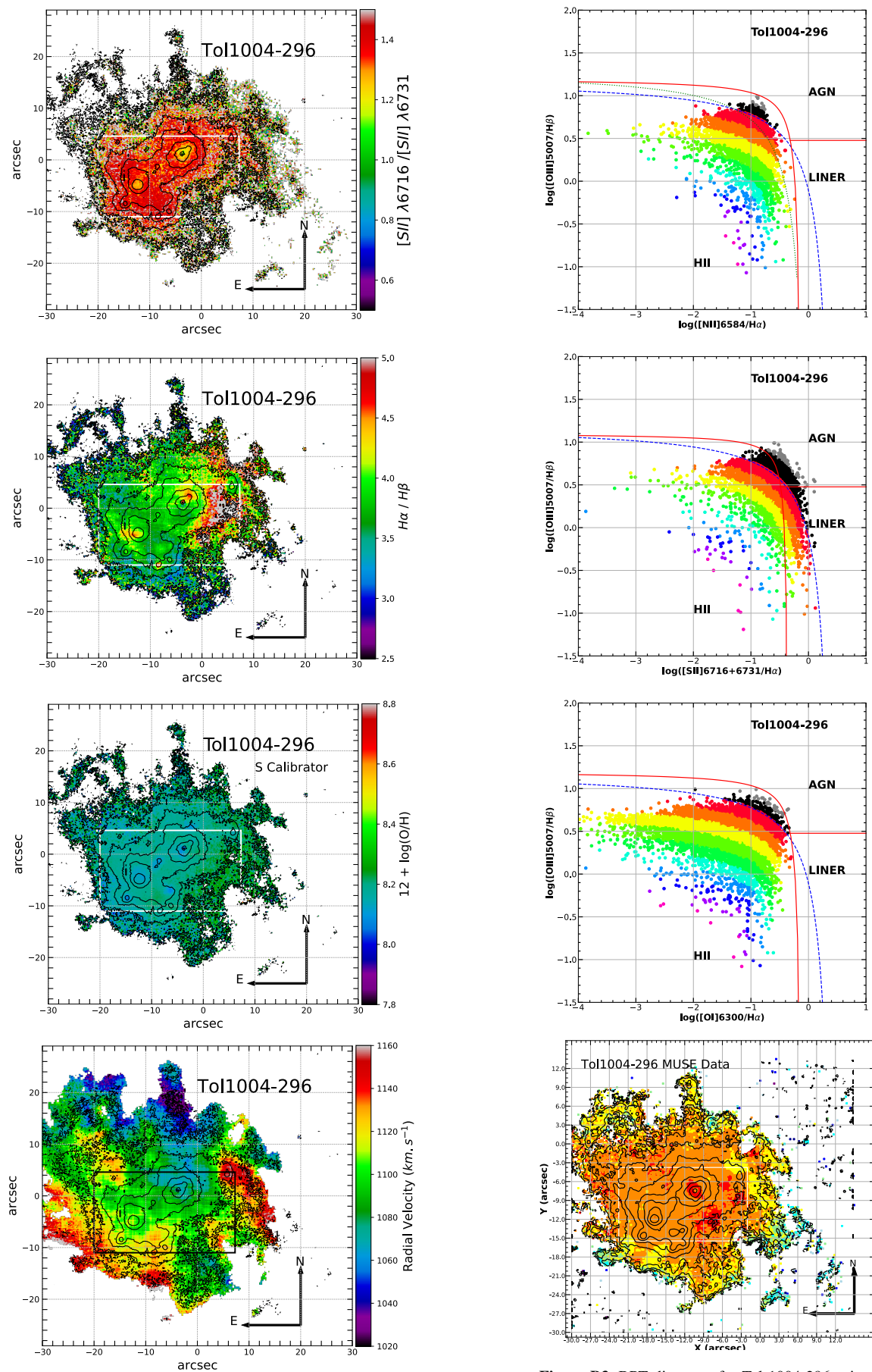


Figure B1. Tol 1004-296 MUSE data - Monochromatic Maps. Rectangle represents SIFS FoV.



**Figure B3.** Tol 1004-296 MUSE data: From Top to Bottom:  $[SII]\lambda 6716/\lambda 6731$  Amap (electron Density);  $H\alpha/H\beta$  map (Extinction); Metallicity map (S Calibrator); Radial Velocity Map. Rectangle represents SIFS FoV.

**Figure B3.** BPT diagrams for Tol 1004-296 using the MUSE data. Colors represent the distance from the [Kewley et al. \(2001\)](#) separation (blue dash line). Red lines represent separation from [Veilleux & Osterbrock \(1987\)](#). Bottom map represents the spatial location of the different points from the  $[OIII]5007/H\beta$  vs  $[NII]6584/H\alpha$  diagram. Rectangle represents SIFS FoV.